machines

MDPI

Article

Co-Rotational Auto-Resistance Mechanism and Load-Adaptive Recommended Switching Timing Strategy for Dual-State Operation of Single-End Segmented Rotor Induction Machines

Mengxia Cai [1,*], Chaohao Kan [1], Haihong Huang [1], Xinmai Gao [2] and Danlu Yu [1]

[1] School of Electrical Engineering and Automation, Hefei University of Technology, Hefei 230009, China; 2011800036@hfut.edu.cn (C.K.); 2003800057@hfut.edu.cn (H.H.); 2023010046@mail.hfut.edu.cn (D.Y.)
[2] National Key Laboratory of High-Speed Maglev Electromagnetic Vehicle Technology, CRRC Qingdao Sifang Co., Ltd., Qingdao 266000, China; gaoxinmai@cqsf.com
* Correspondence: 2022110347@mail.hfut.edu.cn

Abstract

Modern intermittent electromechanical drive systems demand reliable heavy-load startup capability, while conventional squirrel-cage induction machines suffer from an inherent trade-off between high starting torque and severe transient inrush current. The single-end segmented rotor induction machine adopts a dual-state operating mechanism to effectively alleviate this contradiction. However, existing studies mainly focus on static electromagnetic performance verification, and load-adaptive recommended switching timing for dynamic operating scenarios remains insufficiently explored, restricting its practical engineering application. This paper addresses this research gap by investigating load-matched switching timing strategies for the proposed dual-state machine. Theoretical modeling of the dual-state operating principle and multi-branch equivalent circuit is performed, combined with finite element simulations and prototype experiments to characterize transient startup and state-transition behaviors at different switching instants and variable loads. The results confirm that the proposed machine reduces startup inrush current by nearly 30% and improves the starting torque multiple by 20% compared with conventional counterparts, based on equivalent-circuit and finite-element analyses. Verified switching rules indicate that pre-synchronization switching best balances light-load transients, whereas under heavy load the winding should be switched as early as the current constraint permits, since delayed switching neither reduces the surge nor shortens startup. This work provides a feasible technical basis for the high-reliability engineering deployment of segmented rotor induction machines in intermittent heavy-load drive systems.

Keywords: single-end segmented rotor; induction machine; dual-state operating; electromagnetic performance; starting torque; switching timing

Check for updates

Academic Editor: Mohamed N. Ibrahim

Received: 3 September 2026
Revised: 18 October 2026
Accepted: 19 October 2026
Published: 21 October 2026

Copyright: © 2026 by the authors. Licensee MDPI, Basel, Switzerland. This article is an open access article distributed under the terms and conditions of the Creative Commons Attribution (CC BY) license.

1. Introduction

Modern special electromechanical drive systems for unmanned mobile equipment widely require long-term static standby and intermittent short-time heavy-load startup operation, which imposes rigorous demands on motor starting torque capability, inrush current suppression and transient operating stability [1,2]. In such variable and harsh operating scenarios, the drive motor must reliably output sufficient torque to overcome static load resistance during startup [3], while avoiding excessive transient inrush current

that impacts the on-board energy storage and electronic control system [4], which is critical to the operational safety and service life of the entire electromechanical system [5].

Permanent magnet synchronous machines (PMSMs) exhibit excellent electromagnetic performance and are widely applied for high-power-density drives [6,7]. Various improved topologies have been proposed to optimize their starting performance [8–10]. However, certain application constraints exist for PMSMs under long-term standby and repeated heavy-load startup conditions [11,12]. Accordingly, high-reliability excitation-free drive motors are highly desirable for special electromechanical propulsion systems with demanding heavy-load startup requirements.

As mature and reliable excitation-free drive devices, induction machines are widely applied in industrial systems owing to their simple structure, low cost and high operational robustness [13,14]. Benefiting from their high environmental adaptability and fault tolerance, induction machines have gradually become promising alternatives for special mobile propulsion equipment. Wound-rotor harmonic-start induction machines have been investigated to enhance starting performance in the context of energy-saving development via theoretical analysis and prototype tests [15–19]. However, conventional wound-rotor machines rely on a brush–slip-ring assembly to access the rotor windings. The brushes and slip rings are subject to continuous wear and require frequent routine maintenance [20,21], and have been identified as a principal failure mode [22], leading to the highest operation and maintenance costs among variable-speed generator systems [23] and severely limiting the applicability of wound-rotor machines in harsh or remote environments [24]. In comparison, squirrel-cage induction machines (SCIMs) possess a simpler structure, lower manufacturing cost and higher mechanical reliability [25], showing prominent application advantages in short-time intermittent drive scenarios. For such operating conditions, the motor only works in the early thermal transient stage during startup, and the slight degradation of steady-state efficiency caused by increased rotor resistance can be basically ignored [26], which further highlights the application potential of SCIMs in special intermittent propulsion systems. Even so, the inherent excessive starting current defect of traditional SCIM topologies still restricts their large-scale engineering promotion [27].

For squirrel-cage induction motors, multiple technical routes have been reported to tackle the inherent trade-off between high starting torque and large starting inrush current. Existing rotor-oriented optimizations include adopting special alloy rotor bars and end-rings, which improve starting performance but increase manufacturing cost [28]; reducing end-ring thickness to raise starting torque, accompanied by higher slip and current harmonic distortion [29]. Despite these efforts, few existing solutions can simultaneously satisfy high starting-torque output, restrained inrush current, favorable steady-state efficiency and low manufacturing cost for intermittent heavy-load startup missions.

Our research group has previously presented a single-end segmented squirrel-cage induction motor based on a co-rotational harmonic field and auto-resistance enhancement mechanism [30]. In this prior work, topological design, electromagnetic finite element simulation and prototype static-performance tests were completed. The machine can realize harmonic starting mode and fundamental-wave steady-state mode. Under harmonic starting, multi-pole-pair co-rotating harmonic fields produce high starting torque, and the segmented-rotor-bar potential-difference effect equivalently increases stator-referred rotor resistance for inrush-current suppression. Previous work verified that this topology achieves improved starting characteristics while keeping steady-state performance comparable with conventional SCIMs of identical frame size.

Nevertheless, existing research only focuses on topological innovation and static performance verification, while neglecting the dynamic state-switching regulation mechanism adapted to intermittent short-time startup operating characteristics, which is the key to

practical engineering application. The dual-state operation of the proposed machine relies on winding switching to realize the transition from harmonic starting to fundamental-wave steady-state operation, and the switching timing directly determines the transient current impact, torque dynamic response and speed pull-in stability of the drive system. Improper switching moments will cause excessive peak current and unsmooth torque output, or prolonged startup time and increased energy consumption, seriously affecting the comprehensive operating performance of the electromechanical drive system. At present, there is a lack of quantitative research on load-adaptive recommended dual-state switching timing strategies for segmented rotor induction machines, forming a major bottleneck restricting the transformation of this novel topology from theoretical research to engineering application.

Different from the previous static performance verification research, this paper further supplements and extends the existing research system, focusing on the dynamic switching optimization of dual-state segmented rotor induction machines under variable-load conditions for special intermittent propulsion drive scenarios. Firstly, the equivalent circuit models and torque–slip characteristics under dual operating states are derived to reveal the electromagnetic-transient mechanism of state switching. Secondly, a high-precision finite element simulation model is established to quantitatively analyze the influence of switching instants on starting current suppression, torque ripple and speed synchronization performance under different load conditions. Finally, multi-condition prototype experiments are carried out to summarize the load-adaptive recommended switching control strategy. This work expands the research of segmented rotor induction machines from topological design and static performance evaluation to dynamic regulation optimization, providing a feasible technical scheme for the high-reliability engineering application of such novel dual-state drive machines. Furthermore, the proposed dynamic switching optimization framework can be extended to various intermittent heavy-load startup drive systems, including auxiliary traction motors for new energy vehicles and mining transport electromechanical equipment, possessing broad engineering application value.

2. Two Operating States of the Prototype Machine

A 3 kW, 380 V four-pole-pair prototype of the single-end segmented squirrel-cage induction machine with a 36-slot stator is manufactured for theoretical analysis and experimental validation. The stator winding configuration and electrical connection topology are shown in Figures 1 and 2, respectively. The stator windings follow standard industrial fabrication processes, ensuring favorable manufacturability and scalability for practical engineering applications. The 36-slot stator integrates two independent winding branches, namely the main winding (subscript d) and the auxiliary winding (subscript a). In steady-state operation, the two branches are connected in parallel and supplied by a unified power source. Based on fundamental electromagnetic principles of induction machines, the two winding branches produce identical fundamental electromotive forces (EMFs) with matched per-phase series turns, i.e., 30 turns for each main coil and 90 turns for each auxiliary coil. The prototype achieves dual-state operation via flexible winding switching. During startup, energizing only the main winding initiates the so-called harmonic starting state, which is intended to enhance starting torque and limit transient inrush current. Once the rotor accelerates to a predefined speed, the auxiliary winding is switched into the circuit, enabling seamless state transition and stabilizing the machine in the fundamental-wave steady-state operating mode.

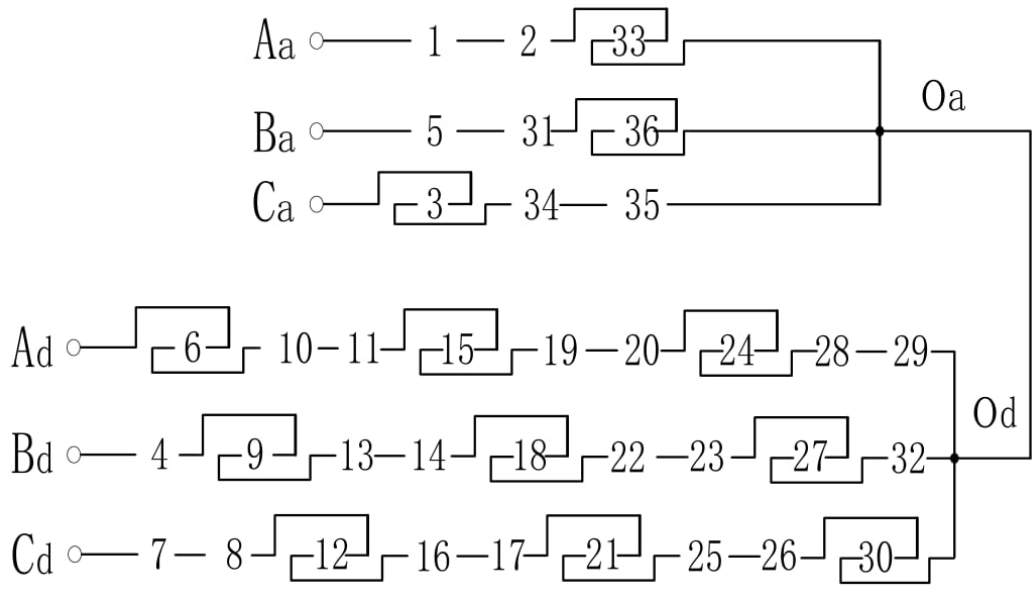


Figure 1. Stator winding configuration diagram.

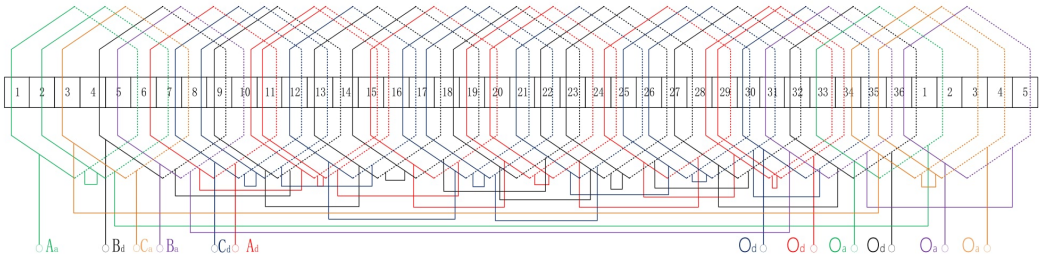


Figure 2. Stator winding schematic.

2.1. Magnetomotive Force Analysis Under Harmonic Starting State

This section employs the slot vector method to investigate the air-gap magnetic field composition and formation mechanism of the proposed single-end segmented squirrel-cage induction machine in the harmonic starting state. During motor startup, only the main winding is energized to excite composite air-gap magnetic fields. To clarify the operating principle of the dual-winding structure, slot vector theory is adopted to quantitatively characterize stator magnetomotive force (MMF) distribution. Each stator slot MMF is abstracted as an independent spatial vector. For a harmonic field with ν pole pairs, adjacent slot vectors present a fixed spatial phase difference. For the 36-slot prototype, this phase difference is defined as $\gamma = \nu(2\pi/36)$, where ν denotes the harmonic pole-pair number. All slot vectors are numbered according to the practical stator layout to form a complete star diagram, and the resultant phase MMF is acquired via vector superposition of corresponding slot vector groups.

The 4-pole-pair fundamental field and the 3-pole-pair and 5-pole-pair harmonic fields are selected as typical cases to plot the slot vector diagrams, as presented in Figure 3, which intuitively demonstrate the synthetic MMF characteristics of different phase winding combinations. Taking the phase-A MMF components of the main winding (*Ad*) and auxiliary winding (*Aa*) in Figure 3a as a representative example, the *Aa* MMF is synthesized by the superposition of slot vectors 1, 2, and −33, while the rest of the slot vectors achieve mutual cancellation. Correspondingly, the *Ad* MMF is formed by the vector summation of slot vectors 19, 20, and −15, and presents a precise 180° phase difference relative to *Aa*. The identical amplitude and reverse-phase relationships can be generalized to the phase-B and phase-C MMF components (*Bd*, *Ba*, *Cd*, *Ca*) of the two winding branches.

Further observation of the slot vector diagrams indicates that the 3-pole-pair and 5-pole-pair harmonic MMFs generated by the main and auxiliary windings consistently feature equal amplitude and opposite spatial phases. In contrast, the 4-pole-pair fundamental MMFs excited by the two winding sets maintain identical amplitude and superimpose in the same spatial direction.

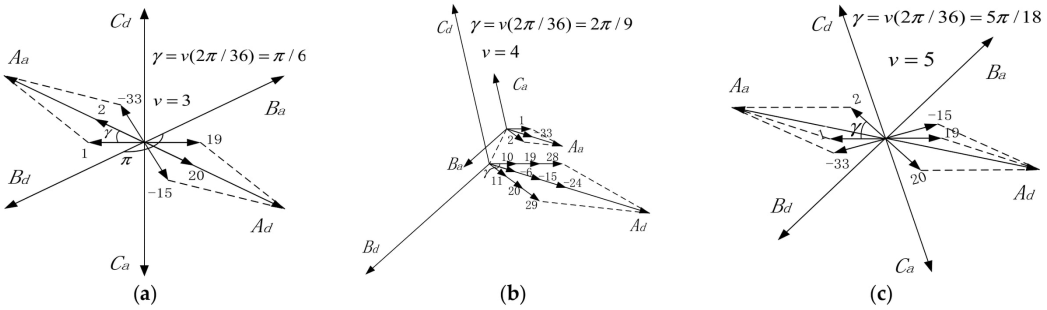


Figure 3. Slot vector diagram of magnetomotive force. (**a**) 3 pole pairs; (**b**) 4 pole pairs; (**c**) 5 pole pairs.

Slot vector analysis confirms that the 3-pole-pair and 5-pole-pair harmonic MMFs generated by the main and auxiliary windings are equal in amplitude and opposite in phase, whereas the 4-pole-pair fundamental MMFs are identical in both amplitude and phase. Under single main-winding excitation for startup, the stator generates superimposed 4 pole-pairs fundamental and 3/5-pole-pair harmonic air-gap fields. This composite multi-pole excitation significantly enhances starting torque output, realizing the high-torque startup advantage of the prototype. In dual-winding parallel steady-state operation, reverse-phase harmonic MMFs from the two branches completely offset each other, while the fundamental magnetic field is positively superimposed. This eliminates air-gap high-order harmonic interference and retains a pure fundamental excitation field, thus guaranteeing stable and high-quality steady-state electromagnetic performance of the proposed machine.

2.2. Electromagnetic Analysis Under Fundamental-Winding Steady-State Operation

The multi-pole-pair composite magnetic field formed in the harmonic starting state contributes to rapid rotor speed pull-in during the startup transient, whereas residual high-order harmonics will degrade the steady-state electromagnetic performance of the machine. Accordingly, after the auxiliary winding is incorporated into the power circuit, the collaborative operation of dual-winding branches is designed to reform a standard 60° phase-band winding configuration, realizing pure fundamental-wave steady-state operation.

The electrical connection principle of the main and auxiliary winding branches is demonstrated in Figure 4. To satisfy reliable parallel operating conditions, the resultant fundamental electromotive force (EMF) of each phase must be identical for the two winding branches. In this analysis, *Nd* and *Na* represent the slot turns of the main winding and auxiliary winding, respectively, and the induced EMF amplitude of a single coil turn is standardized as unit magnitude. The phase EMFs of the main and auxiliary windings can be quantitatively expressed by Equations (1) and (2).

$$\dot{E}_d = 3N_d + 3N_d \cos 20^\circ + 3N_d \cos 20^\circ \tag{1}$$

$$\dot{E}_a = N_a + N_a \cos 20^\circ + N_a \cos 20^\circ \tag{2}$$

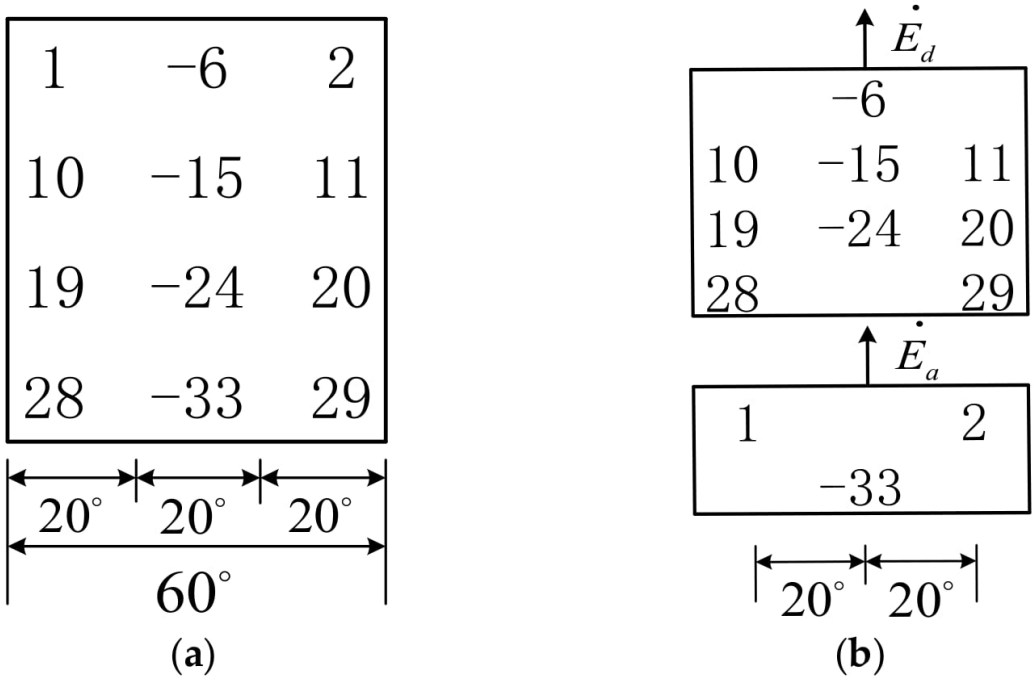


Figure 4. Connection principle of main and auxiliary windings. (**a**) Slot number distribution of Phase-A winding; (**b**) parallel connection of main and auxiliary windings.

Given the practical turn ratio $Na/Nd = 90/30 = 3$, the equivalent relationship in Equation (3) can be further deduced. The derived results verify that *Ed* and *Ea* possess identical amplitude and phase characteristics, which guarantees safe, stable parallel connection and coordinated steady-state operation of the dual-winding branches.

$$\dot{E}_d = \dot{E}_a \tag{3}$$

2.3. Co-Rotational Auto-Resistance Enhancement Mechanism

The stator of the proposed prototype adopts a fixed slot number configuration of $Z_1 = 36$. For a v-pole-pair harmonic magnetic field, the slot MMF of the l-th stator slot can be mathematically modeled via Equations (4) and (5), where N_l denotes the coil turn number of the l-th slot, and θ_l represents the spatial phase angle of the l-th slot relative to the first slot.

$$\dot{F}_l = N_l e^{j\theta_l} \tag{4}$$

$$\theta_l = \frac{2\pi v}{Z_1}(l-1) \tag{5}$$

Taking the *Ad* phase as a typical research object, S_{A_d} is defined as the slot number set occupied by the *Ad* winding. The resultant MMF and corresponding amplitude of the *Ad* phase under the v-pole-pair harmonic field are derived in Equation (6) and Equation (7), respectively.

$$\dot{F}_{A_d v} = \sum_{l \in S_{A_d}} N_l e^{j\theta_l} = \sum_{l \in S_{A_d}} N_l e^{j\frac{2\pi v}{Z_1}(l-1)} \tag{6}$$

$$\left|\dot{F}_{A_d v}\right| = \sqrt{\left[\sum_{l \in S_{A_d}} N_l \cos\left(\frac{2\pi v}{Z_1}(l-1)\right)\right]^2 + \left[\sum_{l \in S_{A_d}} N_l \sin\left(\frac{2\pi v}{Z_1}(l-1)\right)\right]^2} \tag{7}$$

On this basis, the winding factor of the main winding for the v-order harmonic component is defined in Equation (8).

$$k_{wv} = \frac{\left|\dot{F}_{A_d v}\right|}{\sum\limits_{l \in S_{A_d}} N_l} \tag{8}$$

The MMF derivation procedures for the *Bd* and *Cd* phases follow the identical theoretical framework. After obtaining the three-phase MMF vectors $\dot{F}_{A_d v}$, $\dot{F}_{B_d v}$, and $\dot{F}_{C_d v}$, the symmetrical component method is employed to decompose the synthetic MMF field into forward-rotating and backward-rotating components. The rotation factor is defined as $\beta = e^{j120^\circ}$, and the amplitudes of the forward-rotating wave F_{v+} and backward-rotating wave F_{v-} are calculated via Equations (9) and (10).

$$F_{v+} = \frac{1}{3}\left|\dot{F}_{A_d v} + \beta \dot{F}_{B_d v} + \beta^2 \dot{F}_{C_d v}\right| \tag{9}$$

$$F_{v-} = \frac{1}{3}\left|\dot{F}_{A_d v} + \beta^2 \dot{F}_{B_d v} + \beta \dot{F}_{C_d v}\right| \tag{10}$$

Taking the amplitude of the fundamental forward-rotating component F_{4+} as the 100% reference benchmark, the relative proportions of forward- and backward-rotating components for each harmonic order are quantified by Equations (11) and (12).

$$F_{v+}\% = \frac{F_{v+}}{F_{4+}} \times 100\% \tag{11}$$

$$F_{v-}\% = \frac{F_{v-}}{F_{4+}} \times 100\% \tag{12}$$

The statistical percentages of harmonic MMF amplitudes under dual operating states relative to the reference value are summarized in Table 1.

Table 1. Relative forward/backward harmonic contents for various pole pairs.

Pole Pairs	Winding Factor	Forward Rotating Wave Content (%)	Backward-Rotating Wave Content (%)
1	0.04	16.77	6.53
2	0.16	34.57	3.92
3	0.29	41.36	0
4	0.95	100	0
5	0.21	17.76	2.26
6	0.07	5.22	2.61
7	0.01	0.26	0.47

Table 1 quantifies the winding factor and the relative content of forward-rotating and backward-rotating MMF for each pole-pair harmonic under single-main-winding excitation (harmonic starting state), with the amplitude of the forward-rotating fundamental MMF (4 pole pairs) taken as the 100% reference benchmark. The characteristics of each concerned pole-pair component are further elaborated as follows:

4-pole-pair fundamental component: It possesses the highest winding factor of 0.9452 and contains only a forward-rotating component with zero backward-rotating content. As the dominant field component throughout the entire startup process, it provides the base

electromagnetic torque and determines the overall torque level. It is also the only field component retained in the steady-state operation mode.

3-pole-pair harmonic component: It has a winding factor of 0.2932, with a forward-rotating content of 41.36% and zero backward-rotating component. It is the most prominent harmonic component besides the fundamental wave. Benefiting from its lower pole-pair number and correspondingly higher synchronous speed, it maintains a large slip at low rotor speeds, thus delivering significant driving torque in the early startup stage. The absence of a backward-rotating component also avoids additional braking torque.

2-pole-pair harmonic component: It has a winding factor of 0.1634, with 34.57% forward-rotating and 3.92% backward-rotating content. The forward component provides additional driving torque, while the weak backward component introduces negligible braking effect.

1-pole-pair harmonic component: It has a low winding factor of 0.0396, with 16.77% forward and 6.53% backward content. Its overall amplitude is very low due to the small winding factor, so its contribution to the total field is very limited.

5-pole-pair harmonic component: It has a winding factor of 0.2099, with 17.76% forward and 2.26% backward content. In the early startup stage (rotor speed below 600 r/min, i.e., the synchronous speed of the 5-pole-pair field), the slip is positive and it provides positive driving torque. However, when the rotor speed exceeds 600 r/min, the slip becomes negative and the 5th-order harmonic torque converts from driving torque to braking torque. This is the dominant reason for the torque drop in the late stage of harmonic starting, and also the core basis for determining the recommended switching timing.

In summary, the superposition of multiple forward-rotating harmonic fields is the core mechanism for starting torque enhancement. The backward-rotating components of all orders are at a low level overall, so the net braking effect is weak, ensuring a positive net torque gain from harmonic superposition.

3. Parameter Analysis and Performance Investigation Under Variable Operating States

Combined with the harmonic MMF distribution characteristics and co-rotational auto-resistance enhancement principle clarified in the foregoing dual-state electromagnetic analysis, this section further investigates the operating mechanism and parametric performance of the proposed machine. Focusing on the customized stator dual-winding configuration and novel single-end segmented squirrel-cage rotor structure, the rotor equivalent circuit, current distribution law and variable-load electromagnetic torque characteristics are systematically analyzed to reveal the essential mechanism of inrush current suppression and heavy-load starting optimization.

3.1. Operating Principle of Single-End Segmented Rotor Under Dual Operating States

The prototype adopts a 32-slot squirrel-cage rotor with a total rotor bar number of $N = 32$. One end ring is uniformly divided into $Q = 4$ independent segments, where each segmented end ring connects $n = N/Q = 8$ rotor bars, while the opposite end ring remains fully integrated and unsegmented. The equivalent circuit of each rotor bar group is established in Figure 5, where $\dot{E}_m (m = 1 \sim n)$ denotes the segmented induced electromotive force (EMF) of each rotor bar branch, and the non-segmented rotor end (point b) is defined as the reference potential node.

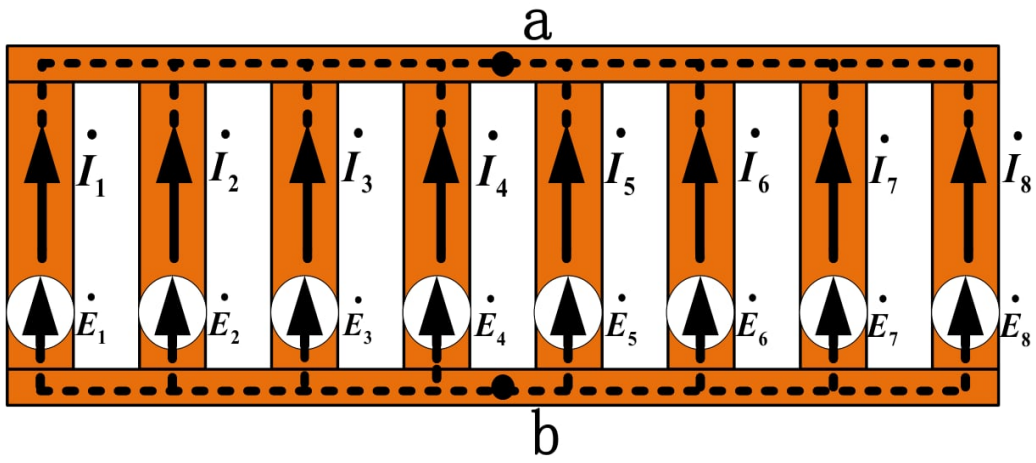


Figure 5. Circuit schematic for one rotor bar group.

When the stator excitation contains a ν-pole-pair harmonic magnetic field, all rotor bars within a single segmented group generate induced EMFs with identical amplitude E and uniform sequential phase difference $\delta = 2\pi v/N$. The potential of the segmented-end node V_a is equivalent to the average EMF value of the corresponding rotor bar group, which is quantitatively characterized by Equations (13) and (14).

$$\dot{V}_a = \frac{1}{n}\sum_{m=1}^{n}\dot{E}_m = k_n E e^{j\frac{(n-1)\pi v}{N}} \tag{13}$$

$$k_n = \frac{Q\sin(\pi v/Q)}{N\sin(\pi v/N)} \tag{14}$$

In this modeling process, the leakage impedance of segmented end connections is neglected for theoretical simplification, and only the rotor bar leakage impedance Z_0 is considered. Accordingly, the transient current of the m-th rotor bar is derived as $\dot{I}_m = \left(\dot{E}_m - \dot{V}_a\right)/Z_0$.

Under the harmonic starting state, the harmonic pole-pair order satisfies $\neq Q$, yielding a non-zero coefficient k_n and non-zero segmented-end potential V_a. This breaks the uniform current distribution among rotor bars and forms asymmetric bar current amplitudes. As visualized in Figure 6, the rotor currents present a symmetrically distributed pattern with larger amplitudes at the two terminal bars and smaller amplitudes in the middle bars of each segmented group. From the stator side, such uneven current distribution equivalently reduces the effective rotor winding turns and increases the stator-referred rotor resistance. The elevated equivalent rotor resistance effectively suppresses the transient starting inrush current and improves the electromagnetic torque output, realizing the core advantages of startup enhancement for the proposed machine.

In the fundamental-wave steady-state operating state, the fundamental magnetic field satisfies $\sin(\pi v/Q) = \sin\pi = 0$, which leads to $k_n = 0$ and further eliminates the segmented-end potential deviation ($V_a = 0$). In this case, the rotor bar current equation is simplified to $\dot{I}_m = \dot{E}_m/Z_0$, and uniform current distribution is achieved across all rotor bars. The segmented rotor structure fails to produce additional resistance enhancement effect under fundamental excitation, and the prototype thereby exhibits consistent electromagnetic characteristics and operating performance with conventional squirrel-cage induction machines.

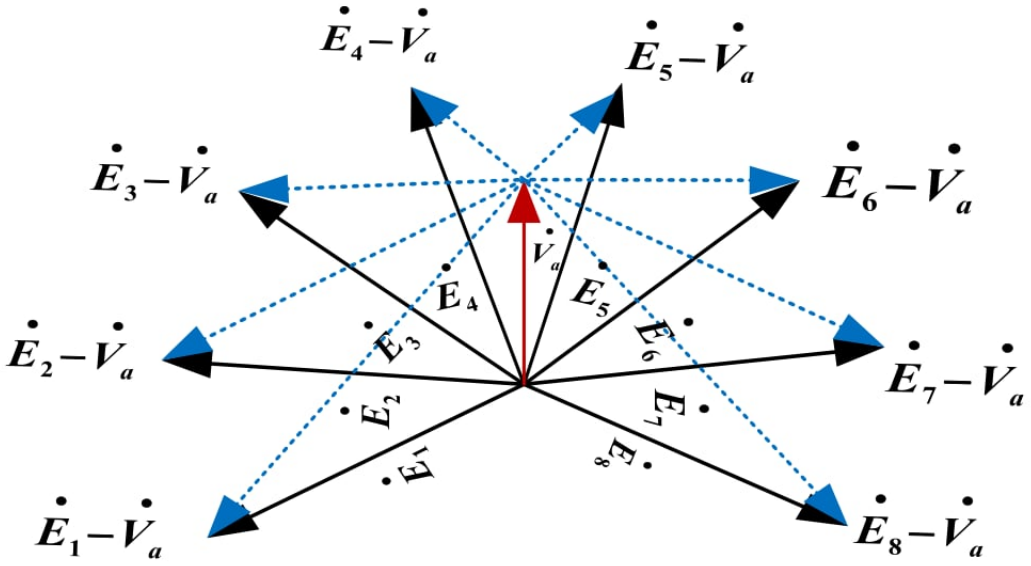


Figure 6. Rotor EMF and current vector diagram for 3-pole-pair harmonic field.

3.2. Equivalent Circuit and Parametric Analysis Under Dual Operating States

According to the differentiated field-superposition characteristics of the proposed machine, the equivalent circuit topology varies significantly under dual operating states. The harmonic starting state adopts a composite equivalent network containing a fundamental-wave branch and multiple independent harmonic branches, while only the pure fundamental-wave branch is retained for the fundamental steady-state operating state. Corresponding equivalent circuit models are established in accordance with the dual-state operating principles, as illustrated in Figure 7.

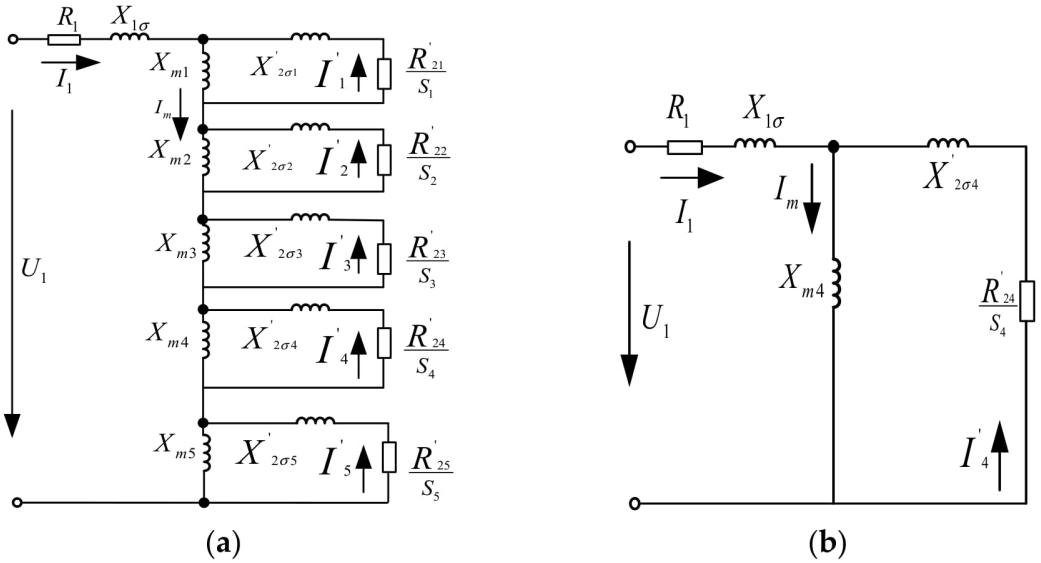


Figure 7. Equivalent circuits under different operating states. (**a**) Harmonic starting state; (**b**) fundamental steady-state operating state.

In the equivalent circuit, U_1 denotes the stator terminal voltage, R_1 represents the stator resistance, and $X_{1\sigma}$ is the stator leakage reactance. X_{mi} indicates the magnetizing reactance corresponding to the i-pole-pair magnetic field. For the i-order magnetic field component, $X'_{2\sigma i}$, R'_{2i}/s_i, and I'_i are defined as the stator-referred rotor leakage reactance, equivalent rotor resistance, and rotor current, respectively. The fundamental pole pair of the prototype is fixed as $p = 4$. Specifically, $s_i (i \neq p)$ denotes the slip between the rotor

mechanical speed and the synchronous speed of the i-pole-pair harmonic field, while s_p represents the fundamental slip, covering the harmonic order range of i = 1~5.

Magnetic fields with different harmonic orders possess distinct synchronous rotational speeds, which necessitates the definition of multi-order slip variables for accurate harmonic-state modeling. Compared with the fundamental steady-state operation, the superposition of multiple harmonic branches increases the total loop impedance of the equivalent circuit during harmonic starting, which fundamentally suppresses the transient starting inrush current and optimizes the machine's transient response characteristics.

To further quantify the rotor harmonic response characteristics, the rotor slot pole ratio is calculated as $\tau = Z_r/2p = 32/8 = 4$, where Z_r is the total rotor slot number. Within a single segmented rotor bar group, the differential current is obtained by subtracting the current of the latter four rotor slots from that of the former four slots, as expressed in Equation (15) with k = 1~4. Substituting the rotor bar current formula $\dot{I}_m = \left(\dot{E}_m - \dot{V}_a\right)/Z_0$ yields the expanded differential current equation in Equation (16). The phasor superposition of all differential current components is further conducted to derive the total resultant rotor current phasor, as shown in Equation (17).

$$\dot{J}_k = \dot{I}_k - \dot{I}_{k+4} \tag{15}$$

$$\dot{J}_k = \frac{\dot{E}_k - \dot{E}_{k+4}}{Z_0} = E\frac{e^{j(k-1)\delta} - e^{j(k+3)\delta}}{Z_0} \tag{16}$$

$$\dot{I}_\Sigma = \sum_{k=1}^{4} \dot{J}_k = \frac{E}{Z_0}(1 - e^{j4\delta}) \sum_{k=1}^{4} e^{j(k-1)\delta} \tag{17}$$

The reference current I_{ref} is defined in Equation (18), where the total resultant current I_Σ is calibrated to be equal to I_{ref} under pure fundamental excitation. On this basis, the relative evaluation index for each harmonic magnetic field is defined in Equation (19), namely the rotor winding factor ratio, which is quantified as the amplitude ratio of the resultant rotor current to the reference current. This evaluation index effectively characterizes the differential response capability of the segmented rotor structure to different-order harmonic fields.

$$I_{ref} = 2\left|\frac{E}{Z_0}\right| \cdot \left|\sum_{k=1}^{4} e^{j(k-1)\delta}\right| \tag{18}$$

$$k_{xd}(v) = \frac{I_{ref}}{I_\Sigma} = \frac{2}{\left|1 - e^{j4\delta}\right|} \tag{19}$$

The calculated rotor winding factor ratio of each harmonic component is summarized in Table 2. The analytical results demonstrate that, under the harmonic starting state, the spatial axis of the rotor-induced magnetic field deviates from the electrical angle of rotor conductors for each segmented bar group. This deviation reduces the resultant MMF amplitude of the rotor bars, which is electrically equivalent to the reduction of effective rotor winding turns. In this case, the stator-referred rotor leakage impedance remains basically unchanged, while the equivalent rotor resistance is significantly increased, effectively improving the machine's power factor. Meanwhile, the critical speed corresponding to the maximum electromagnetic torque decreases, which ultimately realizes the recommended design of starting torque enhancement and transient current suppression for the proposed dual-state induction machine.

Table 2 presents the rotor winding-factor ratio for each harmonic order, which characterizes the modulation effect of the single-end segmented rotor structure on the equivalent rotor impedance of each harmonic field. This ratio is defined as the amplitude ratio of the

resultant rotor current under the segmented structure to that under a conventional uniform cage structure.

Table 2. Rotor winding-factor ratio corresponding to each harmonic component.

Pole Pairs	Rotor Winding-Factor Ratio
1	2.6131
2	1.4142
3	1.0824
4	1
5	1.0824
6	1.4142
7	2.6131

For the 4-pole-pair fundamental field, the ratio is exactly 1, meaning the segmented structure has no additional resistance enhancement effect on the fundamental operating state. This is consistent with the design goal that the steady-state performance of the proposed machine matches that of conventional squirrel-cage induction machines.

For 3-pole-pair and 5-pole-pair harmonics, the ratio is about 1.0824; for 1-pole-pair and 7-pole-pair harmonics, the ratio reaches 2.6131. This indicates that the farther the harmonic order deviates from the fundamental pole-pair number, the stronger the auto-resistance enhancement effect of the segmented rotor.

Physically, the asymmetric bar current distribution caused by segmented end rings equivalently reduces the effective rotor winding turns and increases the stator-referred rotor resistance. This effect not only suppresses the starting inrush current, but also shifts the peak torque point of each harmonic branch to lower speeds, which further improves the low-speed starting torque. This mechanism works synergistically with the multi-harmonic field superposition to jointly achieve the dual advantages of high starting torque and low starting current.

The equivalent circuit is derived under the standard assumptions of cage induction machine modeling, with specific consideration given to the segmented end-ring topology. The end-ring resistance is retained, while the rotor end-leakage impedance is calculated with a simplified uniform formula, as segmentation primarily affects the circumferential current path and has little impact on total end leakage. Inter-bar currents are neglected owing to the high contact resistance between the bars and the laminations. The skin effect is not modeled separately, as shallow-slot copper bars limit its influence at the supply frequency, and the equivalent circuit parameters are calibrated experimentally. The main magnetizing reactance accounts for saturation, whereas the leakage reactance is treated as constant since the leakage paths are dominated by air gaps and non-magnetic regions. Rotor slot leakage is calculated using the classical slot leakage coefficient method, as the slot geometry and bar structure are unaltered by end-ring segmentation.

3.3. Torque Characteristic Analysis Under Dual Operating States

Based on the established multi-branch equivalent circuit model illustrated in Figure 7, the harmonic electromagnetic parameters of the prototype under the harmonic starting state are quantitatively calculated, and the total electromagnetic torque is further solved via Equation (20).

$$\begin{aligned} T &= T_1 + T_2 + T_3 + T_4 + T_5 \\ &= \frac{m}{2\pi f}\left(I'_{1st}{}^2 \frac{R'_{21st}}{s_1} + I'_{2st}{}^2 \frac{R'_{22st}}{s_2}\right. \\ &\left. + I'_{3st}{}^2 \frac{R'_{23st}}{s_3} + I'_{4st}{}^2 \frac{R'_{24st}}{s_4} + I'_{5st}{}^2 \frac{R'_{25st}}{s_5}\right) \end{aligned} \tag{20}$$

In this formula, I'_{ist} and R'_{2ist} denote the stator-referred starting current and equivalent starting resistance, respectively. The total startup electromagnetic torque T consists of the fundamental torque component T_4 and multiple harmonic torque components, where T_1, T_2, T_3, and T_5 represent the electromagnetic torques generated by 1-pole-pair, 2-pole-pair, 3-pole-pair, and 5-pole-pair harmonic fields, respectively.

To ensure the fairness and accuracy of the comparative analysis, the simulation model maintains identical stator structural parameters to the conventional squirrel-cage induction machine with the same power and voltage ratings, with only the stator windings and rotor structure redesigned in the proposed prototype. The key structural and electromagnetic parameters are summarized in Table 3. The parameters of the multi-branch equivalent circuit are summarized in Table 4.

Table 3. Key parameters of the prototype.

Parameter	Value
Rated power/kW	3
Rated voltage/V	380
Rated current/A	9.61
Number of slots	36/32
Pole pairs	4
Stator outer diameter/mm	210
Stator inner diameter/mm	136
Rotor inner diameter/mm	48
Rotor outer diameter/mm	135.2
Core length/mm	115
Wire diameter (main/auxiliary)/mm	0.67/0.67
Parallel strands (main/auxiliary)	3/1
Supply frequency/Hz	50
Synchronous speed/rpm	750

Based on the multi-branch equivalent circuit model illustrated in Figure 7, the results in Figure 8 are derived using the dual-state equivalent circuit and calibrated electromagnetic parameters. The torque–slip (T-s) characteristic curve under the harmonic starting state is plotted in Figure 8a. Furthermore, Figure 8b comprehensively compares the T-s characteristics of the proposed machine under dual operating states and the conventional squirrel-cage induction machine.

The characteristic curves indicate that the prototype exhibits a comparable starting torque multiple to the conventional machine under the fundamental normal starting state. In contrast, the harmonic starting state delivers a prominent torque improvement, with the starting torque multiple reaching approximately 2.4, which is 1.2 times that of the normal starting state and achieves a 20% performance enhancement compared with the conventional scheme, as predicted by the equivalent-circuit and finite-element models.

Table 4. Parameters of the multi-branch equivalent circuit and their sources.

Parameter Category	Parameter Symbol	Value	Extraction Method
Stator side	Stator phase resistance R_1	2.32 Ω	Analytical calculation + DC measurement verification
	Stator leakage reactance $X_{1\sigma}$	2.59 Ω	Analytical calculation (slot + end + harmonic leakage formula)
1rd harmonic branch (1 pole pairs)	Magnetizing reactance X_{m1}	1.31 Ω	Winding factor scaling + FE harmonic field verification
	Equivalent rotor resistance R'_{21}	0.006 Ω	Analytical calculation + FE harmonic field verification
	Rotor leakage reactance $X'_{2\sigma1}$	0.001 Ω	Analytical calculation + winding factor scaling
2rd harmonic branch (2 pole pairs)	Magnetizing reactance X_{m2}	5.57 Ω	Winding factor scaling + FE harmonic field verification
	Equivalent rotor resistance R'_{22}	0.051 Ω	Analytical calculation + FE harmonic field verification
	Rotor leakage reactance $X'_{2\sigma2}$	0.008 Ω	Analytical calculation + winding factor scaling
3rd harmonic branch (3 pole pairs)	Magnetizing reactance X_{m3}	7.96 Ω	Winding factor scaling + FE harmonic field verification
	Equivalent rotor resistance R'_{23}	0.13 Ω	Analytical calculation + FE harmonic field verification
	Rotor leakage reactance $X'_{2\sigma3}$	0.03 Ω	Analytical calculation + winding factor scaling
Fundamental branch (4 pole pairs)	Magnetizing reactance X_{m4}	46.56 Ω	Magnetic circuit calculation + winding factor scaling
	Equivalent rotor resistance R'_{24}	1.19 Ω	Analytical calculation + FE harmonic field verification
	Rotor leakage reactance $X'_{2\sigma4}$	0.27 Ω	Analytical calculation + winding factor scaling
5th harmonic branch (5 pole pairs)	Magnetizing reactance X_{m5}	1.47 Ω	Winding factor scaling + FE harmonic field verification
	Equivalent rotor resistance R'_{25}	0.06 Ω	Analytical calculation + FE harmonic field verification
	Rotor leakage reactance $X'_{2\sigma5}$	0.01 Ω	Analytical calculation + winding factor scaling

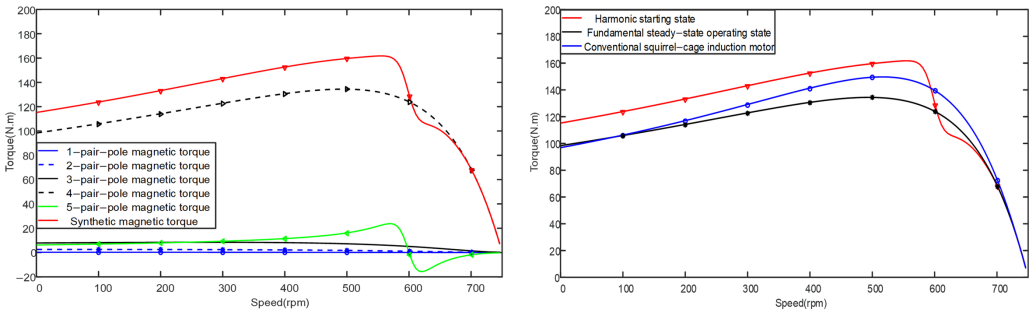


Figure 8. Torque curves in the startup process. (**a**) T–S curve of prototype under harmonic starting state; (**b**) T–s curve comparison between prototype (dual states) and conventional machine.

Nevertheless, in the late startup transient, when the rotor speed approaches the synchronous speed of the 5-pole-pair harmonic field, the 5th-order harmonic torque converts from driving torque to braking torque. This phenomenon reduces the total output torque of the prototype under the harmonic starting state, making it lower than that of the fundamental steady-state operating state. Accordingly, reasonable optimization of the winding state-switching timing is essential to retain sufficient accelerating torque, guarantee smooth and rapid rotor speed pull-in, and complete a high-quality startup transient. This further verifies the necessity of dynamic switching strategy optimization for the reliable and high-efficiency operation of the proposed dual-state induction machine.

4. Finite Element Verification and Dynamic Analysis of Winding Switching

To validate the accuracy of the foregoing theoretical parametric analysis and torque characteristic derivation, a high-fidelity finite-element simulation model is developed in this section. This model is utilized to systematically investigate the transient operating performance under dual working conditions and explore the dynamic electromagnetic characteristics during the winding state switching process. All results presented in the figures within this section are derived from the aforementioned finite-element simulations. The prototype studied in this work is designed on the basis of the co-rotational auto-resistance enhancement mechanism.

4.1. Transient Startup Performance Analysis Under Dual Operating States

All transient finite-element simulations are carried out using Ansys Maxwell 2D transient magnetic solver (ANSYS, Inc., Canonsburg, PA, USA) with fully coupled electromagnetic–circuit–mechanical solution. The axial core length is 115 mm, and axial end effects are compensated by corrected end-leakage reactance in the circuit model. Adaptive meshing with local refinement in the air gap is adopted, with a total of ~120,000 elements, and mesh independence has been verified. The time step is fixed at 0.1 ms, and the Newton–Raphson method is used for nonlinear iteration with a residual convergence criterion of 1×10^{-4}. Stator and rotor cores use D23-50 silicon steel (Changhang Group Wuhan Electric Co., Ltd., Wuhan, Hubei Province, China) with nonlinear B-H curves to account for saturation. The rotor is assumed ideally concentric with zero eccentricity, and the moment of inertia is 0.09 kg·m^2 with a viscous damping coefficient of 0.031 N·m·s/rad. The external circuit is supplied by a 380 V/50 Hz AC source, and winding switching is realized by ideal switches.

No-load transient startup simulations are conducted to compare the current response characteristics of the proposed machine under dual operating states and the conventional squirrel-cage induction machine.

The transient current comparison results are presented in Figure 9. The harmonic starting state yields a peak current of 41.66 A, corresponding to an RMS current of 28.95 A (approximately 3.01 times the rated current). By comparison, the fundamental steady-state produces a higher peak current of 56.84 A, with an RMS value of 38.64 A (around 4.02 times the rated current). For the conventional squirrel-cage induction machine with identical rated specifications, the startup peak current reaches 59.02 A (RMS value of 39.82 A, approximately 4.35 times the rated current). Quantitative calculation demonstrates that the proposed prototype achieves a starting current reduction of nearly 30% under the harmonic starting state compared with the conventional counterpart, verifying its excellent transient current suppression capability.

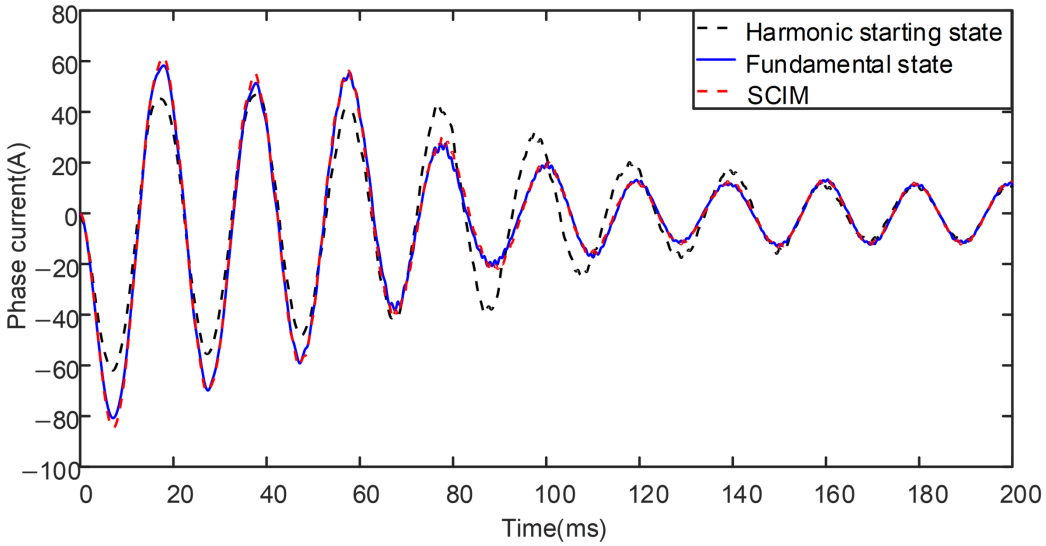


Figure 9. Motor startup current.

Locked-rotor simulation is further performed to accurately quantify the instantaneous startup inrush current. The rotor is mechanically fixed to maintain a zero-speed locked-rotor state, and the locked-rotor current waveforms under dual operating states are obtained, as illustrated in Figure 10. The maximum peak startup current under the harmonic starting state is 42.16 A, while that under the fundamental steady-state operating state is 57.03 A. The locked-rotor test results are highly consistent with the transient startup current data in Figure 9. The above comparative analysis confirms that the harmonic starting state is preferable for the initial startup stage to suppress severe transient inrush current. After the rotor accelerates to a specific speed, switching the machine to the fundamental-wave normal operating state enables coordinated optimization of low-current startup and high-efficiency steady-state operation.

4.2. Transient Performance Analysis of Winding Switching at Variable Instants

To ensure unambiguous interpretation of the transient switching behavior, the following key terms are formally defined with reference to the prototype synchronous speed n_s = 750 r/min. Critical speed: The synchronous speed of the 5-pole-pair harmonic field, calculated as $n_{s,5} = n_s * p/p_5 = 750 * 4/5 = 600$ r/min (80% of n_s). When the rotor exceeds this speed, the 5th-order harmonic torque converts from driving torque to braking torque, as analyzed in Section 2.3 and Figure 8. Pre-synchronization stage: The operating interval in which the rotor has crossed the critical speed and is accelerating toward synchronous speed, but has not yet entered the ±2% settling band. For this prototype, this corresponds to approximately 660–735 r/min (88–98% of n_s). Under no-load conditions, the 150 ms switching instant (~660 r/min) lies within this stage; Post-synchronization stage: The operating state

in which the rotor has reached and remains within the ±2% band of synchronous speed, where switching introduces negligible additional transient disturbance. This corresponds to ≥735 r/min (≥98% of n_s). Under no-load conditions, the 220 ms switching instant (~736 r/min) lies within this stage; Speed pull-in: The transient acceleration process from standstill to synchronous speed (0 → 750 r/min). The pull-in time denotes the duration from startup initiation until the rotor speed first enters and remains within the ±2% band of the target speed (735–765 r/min).

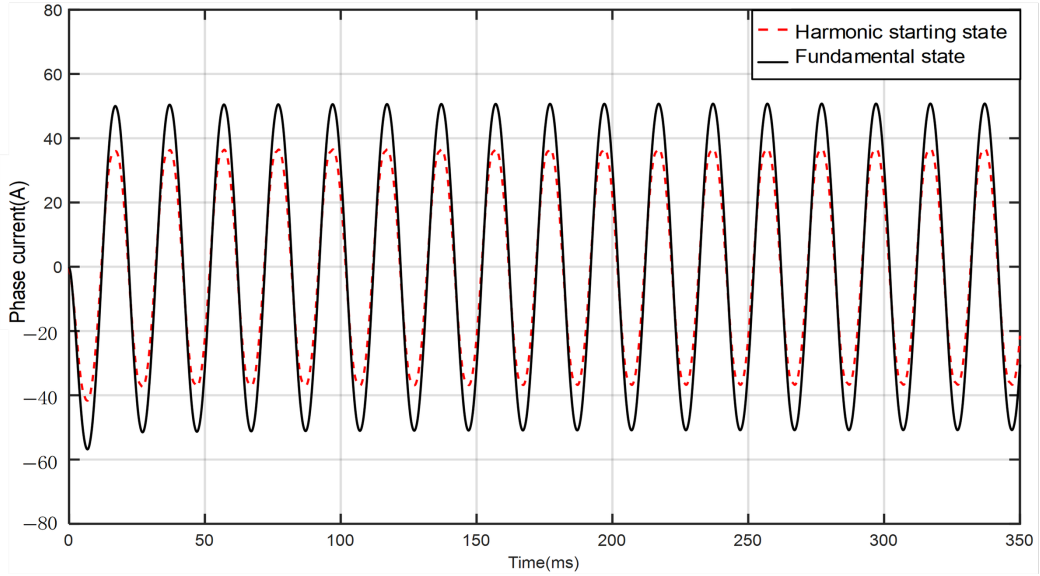
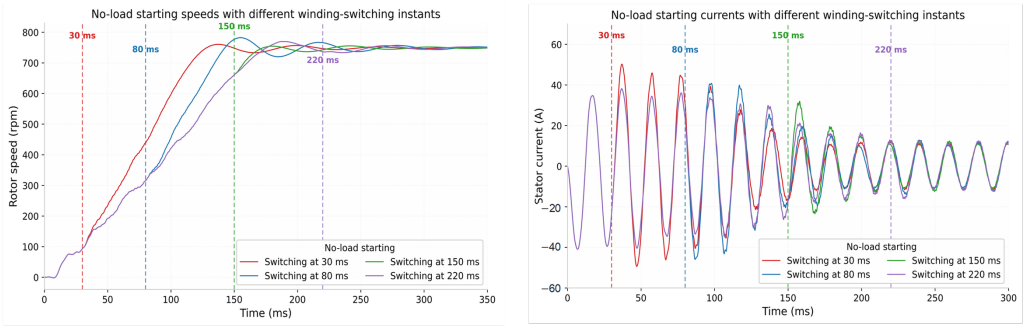


Figure 10. Locked-Rotor current curves under two operating states.

The switching instant is determined by a multi-objective trade-off under two hard constraints: ① Current limit constraint: peak transient current must not exceed the thermal and insulation withstand limits. ② Torque margin constraint: post-switching electromagnetic torque margin must be ≥15% of the load torque. Subject to these constraints, the recommended switching instant aims to minimize the overall transient disturbances (overshoot, settling time, and torque ripple) while maintaining an acceptable startup duration.

The stator branch current during the entire dual-state startup process contains two physically distinct components. The initial startup inrush current is the peak generated during the first voltage application when the machine is energized in the harmonic starting state; this is a natural electromagnetic transient caused by sudden grid excitation of an unmagnetized machine, independent of subsequent winding switching. Under all load conditions, this initial peak is approximately 40 A. The switching-induced additional peak current is the incremental surge that occurs specifically due to the winding state transition (from main-winding-only to main-and-auxiliary-winding parallel); it is measured as the maximum current excursion within the post-switching observation window [t_{sw}, t_{sw} + 50ms]. The 50 ms window captures the complete transient, including the inherent 5–10 ms delay of the current peak relative to the switching instant.

Under no-load conditions, the prototype startup speed characteristic is depicted in Figure 11a. To investigate the switching-induced transient disturbance, four typical switching moments are selected covering the full startup stage: 30 ms (early startup stage), 80 ms (middle startup stage), 150 ms (pre-synchronization stage), and 220 ms (post steady-state synchronization). The corresponding transient stator current waveforms under different switching instants are presented in Figure 11b.



(**a**) (**b**)

Figure 11. No-load switching process at different instants. (**a**) Speed curves; (**b**) current waveforms.

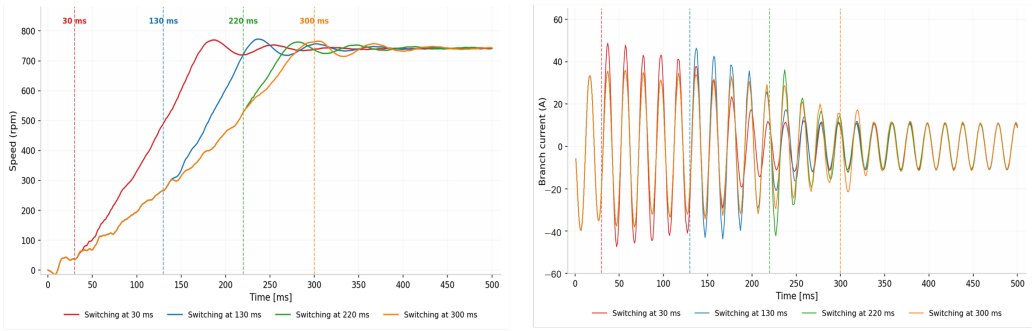
As shown in Figure 11b, the initial inrush appears as the first high peak (~40 A) in all current waveforms; the subsequent peaks correspond to the switching-induced additional surges reported in Table 5. Under no-load conditions, four representative switching instants are compared. Early switching at 30 ms produces a stator transient current peak of 50.0 A at 37 ms: although the fastest speed pull-in is realized, with a startup settling time of 124 ms (post-switching: 94 ms) and a speed overshoot of +1.39% (peak 760.4 r/min at 137.5 ms), the switching surge superimposes on the initial inrush. Switching at the middle startup stage (80 ms) reduces the peak current to 45.9 A at 87 ms, with a startup settling time of 221 ms (post-switching: 141 ms) and an overshoot of +4.4% (peak 782.3 r/min at 155.0 ms). Switching at the pre-synchronization stage (150 ms) yields a peak current of 31.8 A, a startup settling time of 166 ms (post-switching: 16 ms), and a minimal overshoot of +0.9% (peak 755.5 r/min at 239.7 ms). Switching at the post-synchronization stage (220 ms) produces the lowest peak current of 16.1 A and first settles at 197 ms, before switching at 220 ms; the rotor speed reaches a natural peak of 769.6 r/min at 187.8 ms prior to switching under the harmonic starting state, then declines to approximately 735 r/min before the 220 ms switching instant, after which the speed recovers smoothly to the steady-state value of 748.9 r/min without appreciable overshoot. In summary, pre-synchronization switching achieves a favorable balance between low transient current inrush and fast dynamic response for light-load operation.

Table 5. Peak inrush current at different switching instants.

Load Condition	Switching Instant/ms	Total Startup Peak Current/A	Switching-Induced Additional Peak Current/A	Startup Settling Time/ms	Post-Switching Settling Time/ms	Time Saved/ms
No-load	30	50.0	50.0	124	94	73
	80	45.9	45.9	221	141	−24
	150	~40	31.8	166	16	30
	220		16.1	197	22	—
Half load	30	48.8	48.8	235	205	46
	130	46.4	46.4	284	154	−3
	220	42.3	42.3	267	47	14
	300	~40	21.4	281	49	—
Rated Load	30	51.5	51.5	340	310	119
	130	48.3	48.3	338	208	121
	220	49.0	49.0	459	239	—
	300	49.5	49.5	>500	—	—

The same distinction applies in Figure 12b: the ~40 A initial peak is the startup inrush, while the subsequent peaks are switching-induced surges. To investigate the load-adaptive

behavior, half-load tests at 30, 130, 220 and 300 ms are further conducted. At this load level, the harmonic starting state alone is capable of pulling the rotor close to the synchronous speed: the unswitched rotor reaches approximately 764 r/min by 300 ms, in contrast to the rated-load case where the speed remains below 350 r/min at the same instant. Consequently, the switching surge decreases monotonically with the switching instant under half load—48.8 A (30 ms), 46.4 A (130 ms), 42.3 A (220 ms) and only 21.4 A (300 ms, switched at 764 r/min). The corresponding startup settling times are 235 ms (30 ms, post-switching: 205 ms, overshoot +3.9%), 284 ms (130 ms, post-switching: 154 ms, overshoot +4.2%), 267 ms (220 ms, post-switching: 47 ms, overshoot +2.6%), and 281 ms (300 ms, first settles at 281 ms before switching, post-switching: 49 ms, overshoot +3.3%). Half-load operation therefore offers a genuine trade-off: earliest switching maximizes rapidity with an acceptable surge, whereas switching near the pre-synchronization window minimizes the current impact at the cost of a prolonged startup.



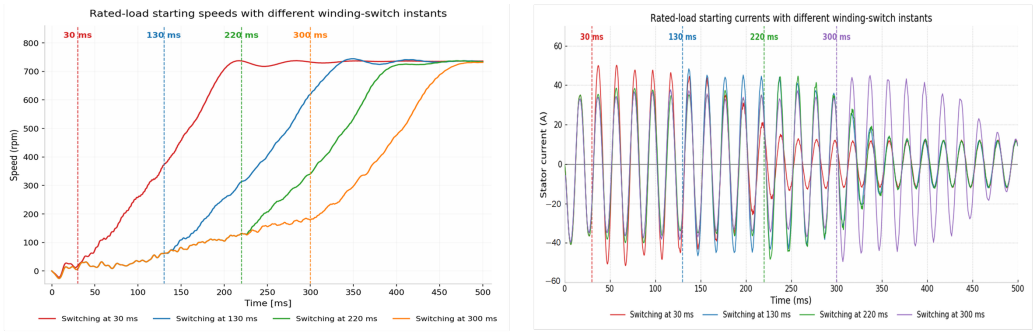
(**a**) (**b**)

Figure 12. Half-load switching process at different instants. (**a**) Speed curves; (**b**) current waveforms.

Similarly, Figure 13b shows the ~40 A initial inrush followed by the switching surges at the respective instants. Under rated-load conditions, the startup duration is further prolonged, and the conclusion differs fundamentally. The rotor speed at the candidate switching instants remains very low (approximately 18, 61, 132 and 179 r/min at 30, 130, 220 and 300 ms, respectively), because the pre-synchronization window is not reached until approximately 420 ms. The corresponding switching surges are 51.5 A, 48.3 A, 49.0 A and 49.5 A—almost independent of the switching instant, since the rotor electromagnetic state at all these instants is similarly far from synchronization. Delaying the switching instant under rated load therefore neither suppresses the inrush current nor shortens the startup. The corresponding startup settling times are 340 ms (30 ms, post-switching: 310 ms, overshoot +0.2%), 338 ms (130 ms, post-switching: 208 ms, overshoot +1.1%), 459 ms (220 ms, post-switching: 239 ms, overshoot +0.9%), and exceed 500 ms (300 ms, overshoot +12.3%, unstable). Rated-load operation should thus adopt the earliest current-safe switching instant (approximately 30 ms), whose surge (~51 A) is comparable to the normal-startup peak current of conventional machines and does not impose additional thermal stress beyond the initial inrush.

As shown in Figure 14, the two-parameter sigmoid law captures the twelve FE points with R^2 = 0.963 and RMSE = 2.21A (6.2% of the data span), well within accepted tolerances for empirical electromagnetic-transient modeling. And the most important finding is that the switching-induced surge current is a single-valued sigmoid function of the rotor speed at the switching instant, essentially independent of the load level itself. All 12 data points collapse onto one curve: $I_{surge} \approx 4 + 45/[1 + e^{(n-691)/95}]$, where n is the rotor speed (r/min) at the switching instant. This law reveals that the load torque affects the surge only indirectly—by governing how quickly the rotor traverses the speed range—not by altering the electromagnetic surge physics at a given speed. Consequently, the behavior at

any intermediate load (e.g., 25% or 75%) can be reliably inferred from this unified curve once the speed trajectory of that load is known, without requiring exhaustive parametric sweeps at every load level.



(**a**) (**b**)

Figure 13. Switching process at different instants under rated load. (**a**) Speed curves; (**b**) current waveforms.

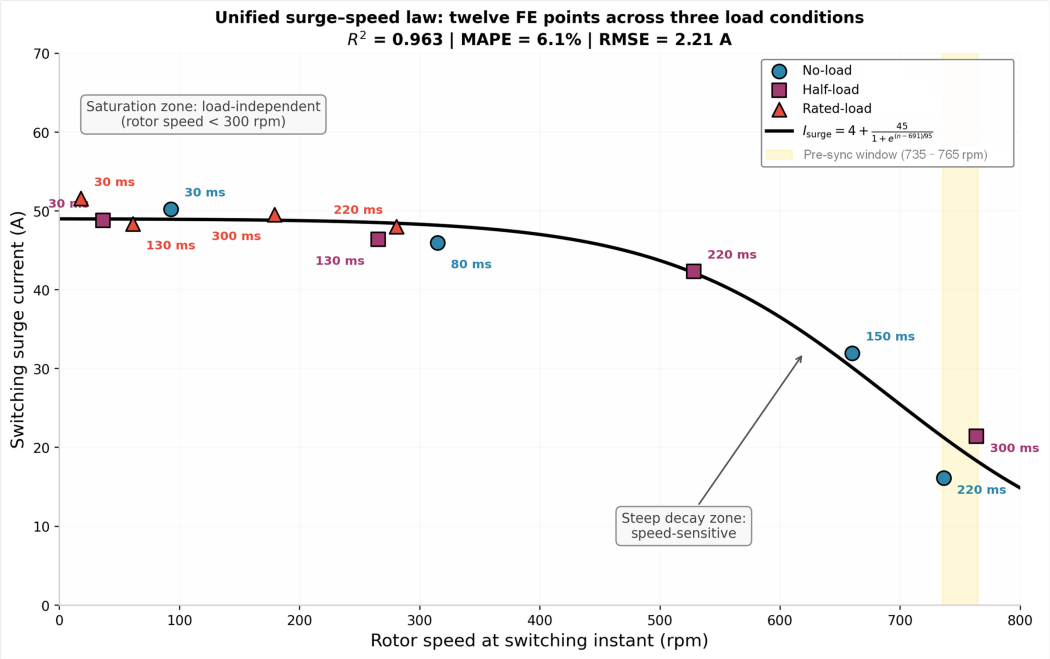


Figure 14. Unified law.

Based on this, the recommended switching strategy is load-adaptive rather than a single linear switching-time relationship: for light loads, switch within the pre-synchronization window (e.g., 150 ms); for heavy loads, switch as early as permitted by the current constraint, since the pre-synchronization window is not reachable in a reasonable time; and for intermediate loads, either the earliest instant (rapidity priority) or the pre-synchronization window (current priority) may be selected.

The switching-induced additional peak current is the maximum current strictly within the post-switching window $[t_{sw}, t_{sw} + 50\text{ms}]$, representing the incremental surge attributable to the switching action. The total startup peak current is the maximum of the initial inrush and the switching-induced additional peak current, rather than asserting it is always the initial inrush. Startup settling time (t_{set}, startup): The time from initial energization (t = 0) until the rotor speed first enters and remains within the ±2% band of the target synchronous speed (735–765 r/min). This quantity describes the overall speed pull-in process. Post-switching settling time (t_{set}, post): The time from the switching instant (t_{sw})

until the speed re-enters and remains within the ±2% band after the switching disturbance. This quantity specifically quantifies the recovery from the switching transient.

The switching-induced surge is caused by the abrupt change in equivalent circuit parameters rather than by cold-start energization. Under post-synchronization switching (e.g., 220 ms no-load, 300 ms half-load), the rotor is near synchronous speed with small slip, so the additional surge is minimal (16–22 A), well below the initial inrush. Under rated load, the surge remains saturated at ~49–51.5 A regardless of switching instant, because all candidate instants occur at low rotor speed with similarly large slip.

The transient current amplitudes under diverse load conditions and switching instants are statistically summarized in Table 5, providing quantitative data support for the formulation of load-adaptive recommended switching strategies.

To further justify the selection of the switching instant, the electromagnetic torques under different switching times are compared in Figure 15. The electromagnetic torque waveforms for all four switching cases (30 ms, 80 ms, 150 ms and 220 ms) are presented in Figure 15. To quantify the torque fluctuation during the post-switching transient process, the absolute pulsation amplitude is defined as $\Delta T = T_{max} - T_{min}$, where T_{max} and T_{min} are the maximum and minimum torque, respectively, over the post-switching interval [t_{sw} + 10 ms, t_{sw} + 100 ms]. This interval is referenced explicitly to the switching instant: the 10 ms offset excludes the spike pulse caused by the voltage step at the switching instant, while the 100 ms upper bound captures the complete decay of the switching-induced transient without including the long-term steady-state ripple.

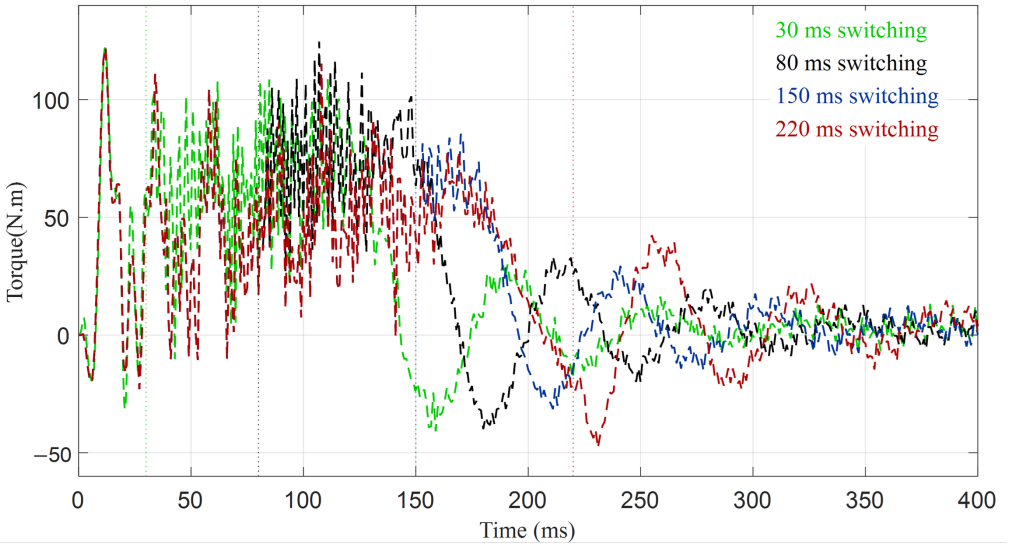


Figure 15. Comparison of electromagnetic torque under different switching times (no-load).

As shown in Table 6, the calculated pulsation amplitudes are 112.46 N·m, 137.18 N·m, 97.44 N·m and 75.23 N·m for the 30 ms, 80 ms, 150 ms and 220 ms cases, respectively. It should be emphasized that the 150 ms recommendation for no-load operation is selected as the Pareto-optimal trade-off among competing objectives—not because it yields the smallest torque pulsation alone. While 220 ms produces lower torque disturbance, its total startup settling time is longer. The 150 ms instant sits at the lower edge of the pre-synchronization window (~660 rpm), where the unified surge-speed law predicts the first substantial current suppression relative to the low-speed saturation level. Switching at this instant captures the dominant electromagnetic benefit—current reduction from the saturated ~49 A regime into the 30 A range—while maintaining a startup settling time comparable to the fastest stable case. Thus, 150 ms represents the earliest switching instant within the pre-synchronization window that achieves effective transient suppression without unnecessary delay. This

recommendation is load-specific: under half-load conditions, the pre-synchronization window is reached near 300 ms, so the recommended instant shifts accordingly; under rated-load conditions, the pre-synchronization window is unreachable within a practical timeframe, and the surge remains saturated regardless of switching instant, so the earliest current-safe instant (~30 ms) is adopted instead.

Table 6. Torque ripple index at different switching instants.

Switching Instant	Tmax (N·m)	Tmin (N·m)	ΔT = Tmax − Tmin (N·m)
30 ms	102.81	−9.65	112.46
80 ms	103.88	−33.30	137.18
150 ms	71.22	−26.22	97.44
220 ms	35.30	−39.94	75.24

The torque-ripple analysis in Table 6 is presented for the no-load condition because the underlying physical mechanism of post-switching torque disturbance is governed by the harmonic field cancellation process, which is independent of the mechanical load. The 15% post-switching torque margin adopted in the recommended switching strategy is a conservative design assumption based on the following rationale. First, the transient torque pulsation quantified in Table 6 (ΔT ranging from 75.24 N·m to 137.18 N·m across the four switching cases) demonstrates that a buffer is required to prevent the instantaneous electromagnetic torque from dropping below the load torque during the recovery interval. The 15% value is selected to provide this buffer while remaining within the accepted engineering range. Second, a 10–20% torque margin is conventional in induction-machine drive design for heavy-load starting applications; the specific 15% figure falls within this range as a mid-range conservative choice. It should be noted that this margin is a design assumption for switching-strategy formulation; validation of the precise value under loaded switching conditions would require additional testing beyond the scope of the present study.

To further reveal the variation of the spatial harmonic content across the state transition, the air-gap radial flux density distributions before and after the switching instant are extracted from the finite-element model for all four switching cases (30 ms: 12 ms and 90 ms; 80 ms: 60 ms and 141 ms; 150 ms: 132 ms and 210 ms; 220 ms: 201 ms and 282 ms), and a spatial FFT is performed along the air-gap circumference. The resulting spectra are compared in Figure 16. Before switching (harmonic starting state, main winding only), the 3-pole-pair and 5-pole-pair components amount to approximately 4–50% of the 4 pole-pairs fundamental, reaching ~45% in the early-switching cases that are in the deep starting region. After switching (dual-winding parallel fundamental state), these harmonic components drop sharply to 2–6%, decaying significantly, by up to one order of magnitude in the dominant harmonics (e.g., the 3rd harmonic drops from ~45% to ~3–4% at 30 ms and 80 ms). This directly confirms, from the spatial-frequency perspective, that the reverse-phase harmonic MMFs of the two winding branches cancel each other after the state transition, leaving a nearly pure fundamental excitation field, which is the physical essence of the dual-state operating mechanism. Meanwhile, the 4 pole-pairs fundamental component increases from 0.47–0.83 T to 0.63–0.90 T owing to the enlarged total magnetomotive force after paralleling. The 3-pole-pair ratio of 44.8% before switching in the 30 ms case agrees well with the analytical value of 41.36% in Table 1, mutually validating the analytical model and the finite-element simulation.

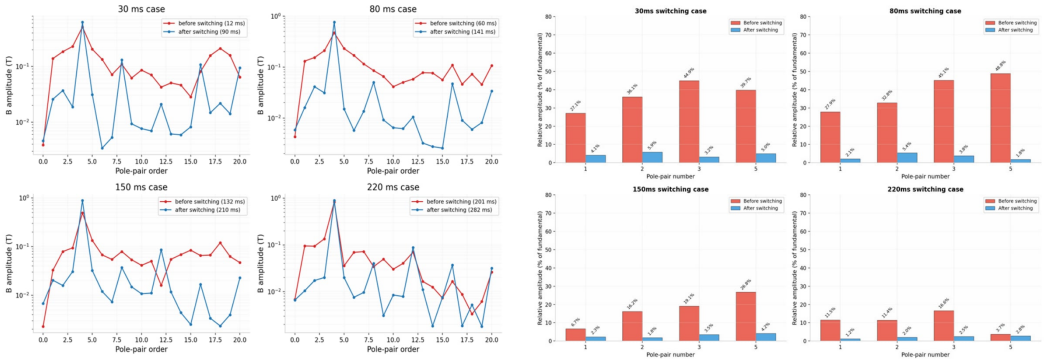


Figure 16. Spatial spectra of the air-gap radial flux density before and after the switching instant for the four switching cases. (**a**) FFT analysis of the radial air-gap flux density; (**b**) percentage of each harmonic component relative to the fundamental component.

Reasonable selection of the winding state-switching timing enables simultaneous suppression of startup inrush current and reduction of overall startup duration, comprehensively improving the transient operational performance and operating reliability of the prototype machine.

5. Experimental Investigation and Validation of the Prototype

On the basis of the foregoing theoretical derivation and finite element simulation analysis, a prototype motor is reconstructed based on a commercial Y132-4 induction motor (Changhang Group Wuhan Electric Co., Ltd., Wuhan, Hubei Province, China) to experimentally validate the transient startup performance and dynamic switching characteristics of the proposed dual-state machine. The key structural and electromagnetic parameters of the prototype are consistent with the simulation model, as listed in Table 3, and the assembled experimental test platform is established as illustrated in Figure 17.

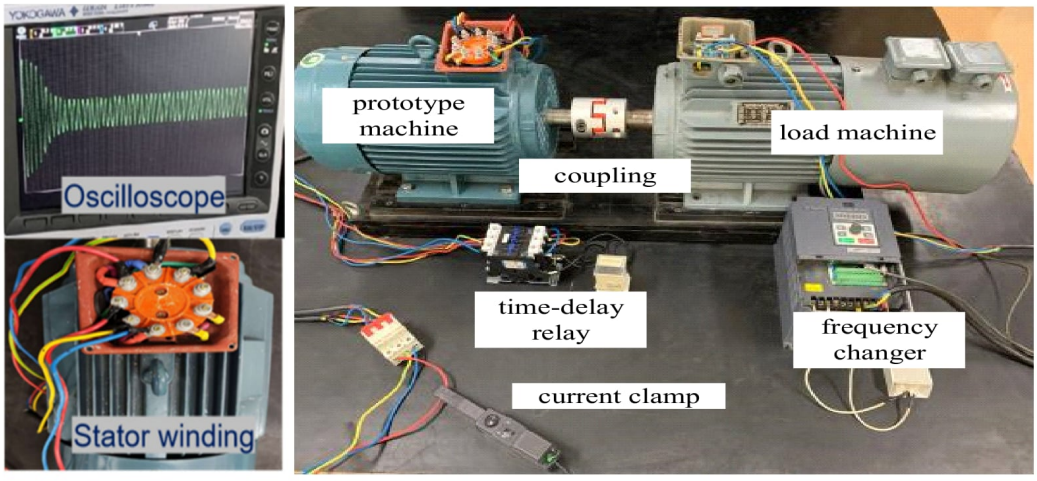


Figure 17. Prototype experimental platform.

An OMRON DH48S-1Z digital time-delay relay is used to control the connection of the auxiliary winding, realizing the transition from harmonic startup mode to fundamental steady mode. The mechanical actuation delay of the relay contact is 2–3 ms, which is the main source of the deviation between experimental and simulated switching instants. Current is measured by a Hall-effect clamp-on current probe with 0–100 A range and 100 kHz bandwidth. Waveforms are recorded by a YOKOGAWA DLM3024 oscilloscope

with a sampling rate of 25,000 S/s. The overall measurement uncertainty of current amplitude is ±1.2%, evaluated in accordance with JJF 1059.1.

For engineering deployment, the load-adaptive switching strategy can be implemented with the practical control scheme of Figure 18, which integrates speed measurement (optional; not required in the prototype), load estimation, switching logic, KM1/KM2 interlocking and protection. The measured speed and the estimated load are compared with the recommended switching-speed relationship of Section 4.2 under the constraints of inrush attenuation and a torque margin of no less than 15%; KM2 is energized only after KM1 is confirmed closed (dead time $\geq$ 10 ms), and any protection trip inhibits the command. The prototype adopts the open-loop time-delay implementation described above, which equivalently realizes the speed threshold under fixed supply and load conditions. Regarding the circulating current between the two parallel branches, the residual EMF difference $\Delta\dot{E} = \dot{E}d - \dot{E}a$ drives $\dot{I}c = \Delta\dot{E}/(Z_1d + Z_1a)$ (Z_1d, Z_1a: stator impedances of the two branches); ideally zero by the balanced branch design (Section 2.2), the practical residual is limited by the branch leakage impedances, is well below the rated current, and no abnormal heating was observed in the prototype tests under the no-load condition.

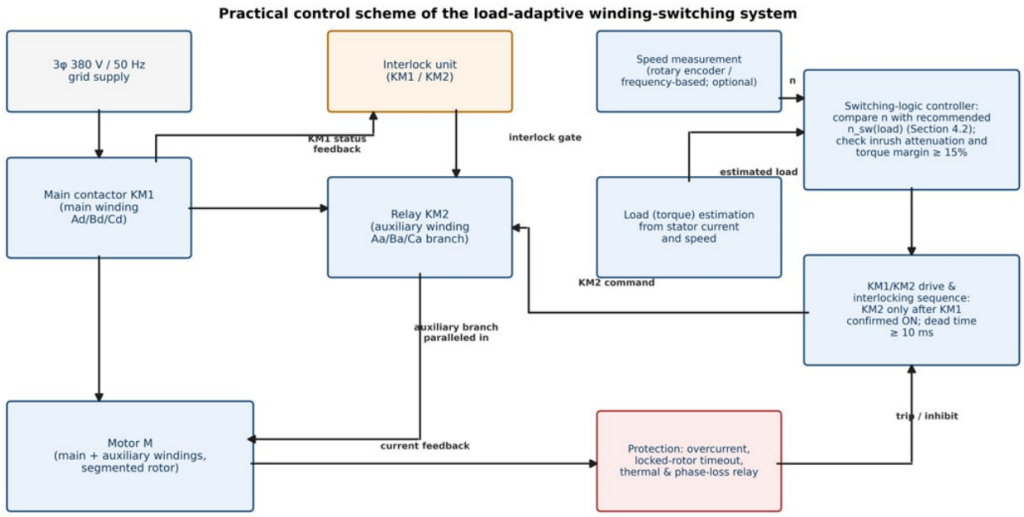


Figure 18. Practical control scheme of the load-adaptive winding-switching system (speed measurement, load estimation, switching logic, KM1/KM2 interlocking, protection, and the parallel-winding transition).

5.1. Experimental Validation of Transient Startup Performance Under Dual Operating States

To verify the accuracy of the simulation results and the feasibility of the topological design, comparative no-load startup experiments are carried out under harmonic starting and fundamental normal starting states. The real-time transient current waveforms under the two operating conditions are captured via oscilloscope measurements, as presented in Figures 19 and 20, respectively.

Experimental waveform analysis demonstrates that the prototype yields a peak phase current of 43.8 A under the harmonic starting state, while the peak phase current reaches 56.5 A under the normal starting state. Relative error calculation is conducted to quantitatively evaluate the consistency between experimental measurements and simulation data. Compared with the simulated current results in Figure 9, the peak current error under the harmonic starting state is approximately 5% and the error under the normal starting state is only 0.5%. The minor discrepancies between experimental and simulated values are mainly attributed to manufacturing tolerance, assembly deviation and measuring instrument errors. The high consistency between experimental and simulation results

effectively validates the correctness of the finite element model and the accuracy of the foregoing theoretical analysis, further confirming that the proposed machine achieves excellent transient current suppression performance under the harmonic starting state while maintaining reliable startup characteristics.

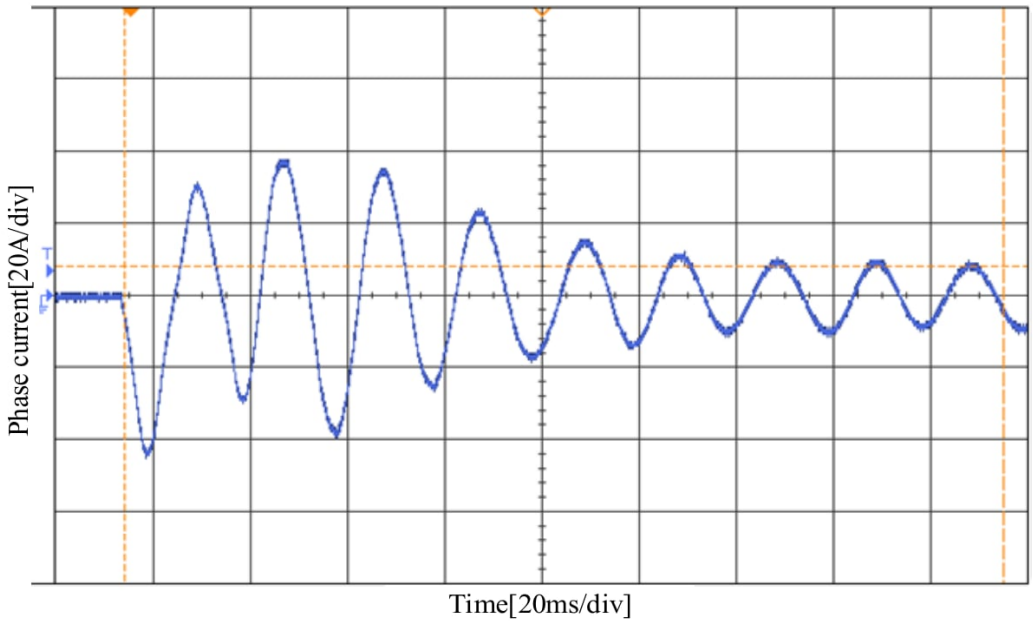


Figure 19. Phase current waveform under harmonic startup.

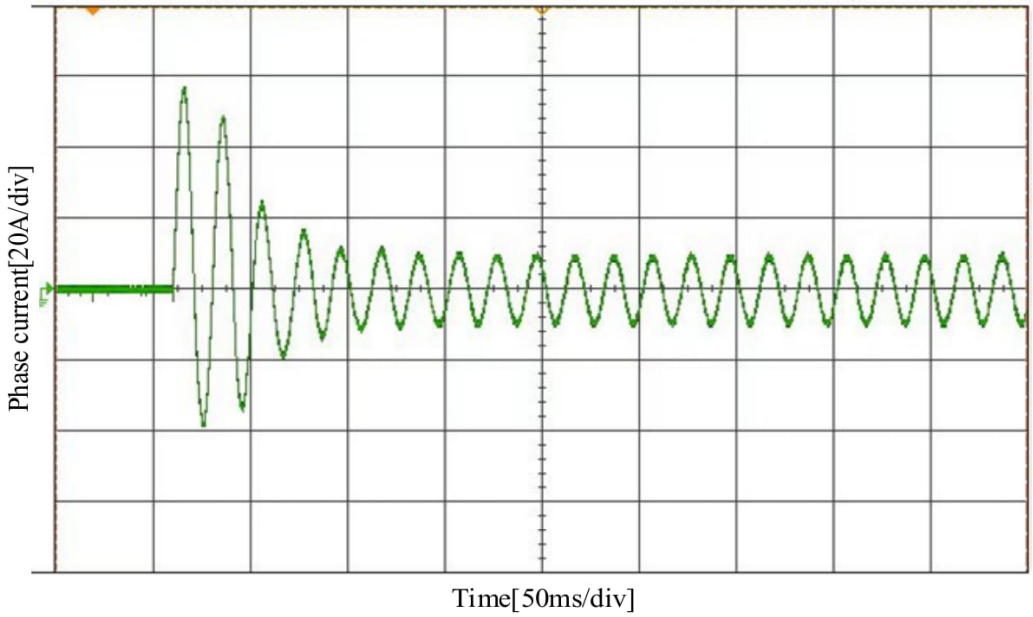


Figure 20. Phase current waveform under fundamental normal startup.

5.2. No-Load Dynamic Switching Experimental Test

To further validate the dynamic transient performance of the dual-state switching strategy under light-load conditions, a no-load winding switching experiment is implemented on the prototype platform. In the test setup, the main winding is directly connected to the grid power supply, while the auxiliary winding is parallel-connected to the main winding terminals through a time-delay relay. Multiple groups of dynamic switching tests are performed by configuring different relay delay timings, and the corresponding stator

transient current waveforms are captured and summarized in Figure 21. The measured current waveforms present deviations from the finite-element simulation results. As stated in the experimental setup, the relay contact actuation delay is 2–3 ms and the current measurement uncertainty is ±1.2% (JJF 1059.1); these are the instrumented experimental constraints. Additional factors hypothesized to contribute to residual discrepancies—core material characteristic variation, winding stacking fabrication error, ambient temperature drift, and relay mechanical inertia—are not directly measured in this setup.

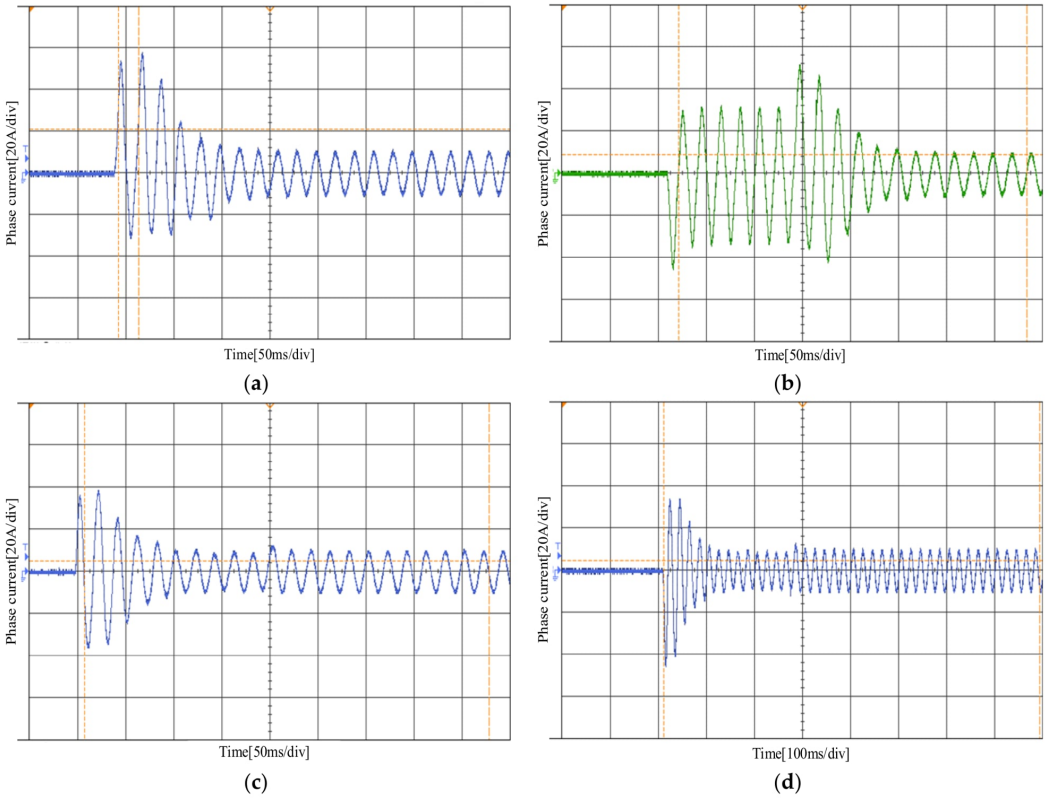


Figure 21. Stator current curves at various switching instants. (**a**) 30 ms; (**b**) 80 ms; (**c**) 150 ms; (**d**) 220 ms.

Experimental measurements indicate that early switching at 30 ms induces a severe transient pulsed current with a peak value of approximately 57 A. When the switching instant is delayed to 80 ms, the peak inrush current is reduced to 51 A. By contrast, switching implemented at 150 ms and 220 ms generates negligible current impact, with peak current limited to approximately 13 A.

For late switching cases such as 150 ms and 220 ms, the initial inrush has largely attenuated to a residual current of approximately 10–12 A (magnetizing current plus decaying DC offset), and the switching-induced surge presents as an incremental peak superimposed on this baseline. The surge amplitude is highly sensitive to the exact switching instant, rotor speed, relay contact dynamics, and parasitic circuit parameters. The relay contact actuation delay causes the actual switching instant to shift backward and the rotor speed to rise slightly, reducing the predicted surge by approximately 2–3 A according to the unified surge-speed law. Additional effects are hypothesized (not directly instrumented) to explain the residual discrepancies: (i) Non-ideal contact closure: Contact resistance (~0.1–0.5 Ω), contact bounce (~1–3 ms), and stray wiring inductance (~2–3 μH) are estimated from manufacturer datasheets and typical electromechanical relay behavior. These parasitic effects are expected to damp the surge relative to the ideal step-change assumption in simulation. (ii) Supply-voltage phase sensitivity: The relay switching is not synchronized with the volt-

age zero-crossing. The 30 ms and 80 ms experimental values, which are moderately higher than simulated, are consistent with unfavorable voltage-phase coincidence; conversely, the 150 ms measurement (~13 A versus 31.8 A simulated) is consistent with favorable phase coincidence combined with contact-bounce damping and superposition on the ~10–12 A residual baseline. This voltage-phase hypothesis is inferred from the amplitude pattern across shots; no synchronized voltage-phase recording is available to confirm it for individual tests. The 220 ms case shows close agreement between simulation (16.1 A) and experiment (~13 A), confirming that the measurement system accurately resolves currents in the 10–20 A range and that the 13 A value reflects a genuine low-amplitude surge rather than a measurement floor. Across all four switching instants, both simulation and experiment exhibit a monotonically non-increasing surge with delayed switching, thereby validating the core theoretical claims: (i) delaying the switching instant reduces the current surge, and (ii) switching inside or near the pre-synchronization window yields minimal electromagnetic disturbance.

To reveal the spectral nature of the switching transient, the measured stator phase currents are analyzed in the time-frequency domain. It should first be clarified that two physically distinct types of harmonics are involved in the switching process. The spatial harmonics characterized by different pole-pair numbers (Section 2.3, Table 1) manifest themselves electrically as low-frequency current components adjacent to the 50 Hz fundamental, namely the slip-frequency components of the corresponding harmonic fields; these components exist throughout the harmonic starting stage regardless of the switching action. In contrast, the temporal harmonics are the non-fundamental current components caused by the abrupt reconfiguration of the winding connection at the switching instant, which corresponds to the equivalent step change of the circuit impedance analyzed by the multi-branch equivalent circuit in Section 3.2.

Since the steady-state THD is only meaningful for periodic waveforms and is not applicable to this short transient process, a short-time Fourier transform (STFT) based time-frequency analysis is adopted. The measured phase currents (25 kS/s) are processed with a sliding Hann window of one fundamental period (20 ms) and 50% overlap, giving a frequency resolution of 50 Hz. The spectrogram of each switching case is aligned to its own switching instant, defined as the power-on instant plus the relay delay setting plus the measured 2–3 ms contact actuation delay, and a uniform relative time window from −20 ms to +80 ms is used for all cases. The resulting spectrograms for the four switching instants are presented in Figure 22.

Three observations can be made from Figure 22. First, the broadband content (150–1200 Hz) observed during the startup process originates from the initial direct-on-line inrush and decays within 40–60 ms; this transient exists in all cases regardless of the switching instant and is a natural property of direct-on-line starting. Second, the winding switching action itself introduces no discernible broadband harmonic emission: at and after the switching instant the spectrum is dominated by the 50 Hz fundamental, and the switching-induced components are confined to low-order frequencies adjacent to the fundamental, decaying within one to two fundamental periods. For the 30 ms early-switching case, the switching instant falls within the initial inrush interval, so the switching surge superimposes on the still harmonic-rich inrush current, which is consistent with its highest measured peak in Table 7; for the 150 ms and 220 ms cases, the inrush has already decayed before switching, and both the time-domain surge (approximately 13 A, Table 7) and the frequency-domain content are minimal. Third, these results are physically consistent with the pre-excited state-transition mechanism analyzed in Sections 3.2 and 4.2: as the winding flux linkage is already established before switching, the transition is far weaker than zero-

state energization, and its spectral signature is a low-amplitude, fast-decaying transient rather than a persistent harmonic pollution.

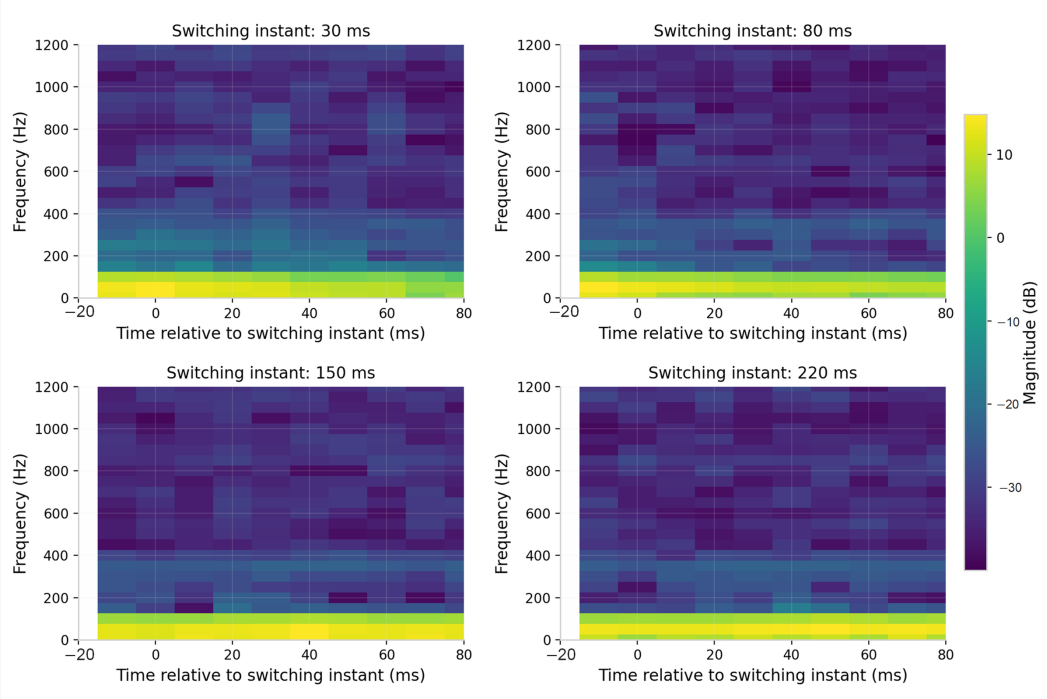


Figure 22. Time-frequency (STFT) spectrograms of the measured stator phase current around the switching instant for the four no-load switching cases.

Table 7. Comparison of simulated and measured switching-induced additional peak currents under no-load condition.

Load Condition	Switching Instant/ms	Simulation Value/A	Experimental Value/A
No-load	30	50.0	≈57
	80	45.9	≈51
	150	31.8	≈13
	220	16.1	≈13

The practical implications of the above spectral characteristics are summarized as follows. Regarding torque ripple, after switching, the air-gap field is dominated by the pure 4-pole-pair fundamental with harmonic components below 6% (Figure 16), and the switching-induced temporal components are of low amplitude and short duration (1–2 fundamental periods). The quantitative torque-ripple comparison across switching instants is provided by the finite-element results in Figure 15 and Table 6. Regarding losses, the additional copper loss of a single switching event, which is proportional to the integral of the squared transient current over the switching interval, is very small according to the measured waveforms; the core loss shows the same trend owing to the short duration of the flux disturbance. Regarding heating, since the switching transient lasts only tens of milliseconds and the additional loss per event is very small, the transient temperature rise of the stator winding is negligible, and the switching transient does not pose a thermal risk for the intermittent short-time duty considered in this work. For applications with extremely frequent switching, cumulative thermal effects deserve attention in future work.

Nevertheless, simulation and experimental results show the same core trend: the later the switching instant, the smaller the additional switching-induced surge. This verifies that switching at the pre-synchronization stage can effectively suppress the transient current,

and therefore this strategy constitutes the recommended switching scheme for the proposed machine under light-load startup conditions.

6. Discussion

The foregoing theoretical analysis, finite-element simulation, and prototype experimental results comprehensively validate the dual-state operating mechanism and load-adaptive switching performance of the single-end segmented squirrel-cage induction machine. Different from conventional squirrel-cage induction machines that suffer from the inherent trade-off between starting inrush current and low-speed torque output, the proposed machine realizes decoupled optimization of transient startup performance and steady-state operation quality through harmonic field superposition and rotor auto-resistance enhancement. The multi-harmonic co-rotating magnetic fields generated by single-main-winding excitation effectively boost the starting torque, while the asymmetric current distribution of the segmented rotor bar group equivalently increases the rotor equivalent resistance, achieving a 30% reduction in startup inrush current compared with conventional counterparts. This core working hypothesis has been fully verified by prior study [30], locked-rotor simulation and transient startup simulation.

The expanded simulation campaign across three load levels—no-load, half-load, and rated-load—reveals that the load torque fundamentally alters the rotor speed trajectory during the harmonic starting stage, thereby changing the electromagnetic state at which winding switching occurs. Under no-load conditions, the harmonic starting state rapidly accelerates the rotor, reaching 660 r/min by 150 ms and 736 r/min by 220 ms; the unswitched rotor even attains a natural peak of 770 r/min at 188 ms before the 5-pole-pair harmonic braking effect pulls it back. Under half-load conditions, the harmonic starting state alone is still capable of pulling the rotor close to synchronous speed, reaching approximately 764 r/min by 300 ms. However, under rated-load conditions, the rotor speed remains very low at the candidate switching instants (approximately 18, 61 and 179 r/min at 30, 130 and 300 ms, respectively), because the accelerating torque is largely consumed by the load torque, and the pre-synchronization window is not reached until approximately 420 ms. This divergence in speed trajectories is the root cause of the qualitatively different switching behaviors observed across the load spectrum.

A key finding from the multi-condition dataset is that the switching-induced surge current is not governed by the load torque itself, but by the rotor speed at the switching instant. All twelve simulated operating points collapse onto a single sigmoid curve described by $I_{\text{surge}} \approx 4 + 45/[1 + e^{(n-691)/95}]$, where n is the rotor speed (r/min) at switching. The surge saturates at approximately 49–51.5 A when switching occurs below 350 r/min, decreases through 42 A near 530 r/min and 32 A near 660 r/min, and falls to 16–21 A within the pre-synchronization window above 735 r/min. This unified law indicates that the load torque affects the surge only indirectly—by governing how quickly the rotor traverses the speed range—while the electromagnetic surge physics at a given speed remain essentially load-independent. Consequently, any intermediate loading level can be addressed through this speed-based criterion without requiring exhaustive parametric sweeps at every load increment.

Based on this unified law, the recommended switching strategy is load-adaptive and formulated as a speed-threshold criterion rather than a single linear switching-time relationship. The following three-zone strategy is derived from the three validated simulation conditions (no-load, half-load, and rated-load), which serve as concrete anchor points across the load spectrum. For light loads (no-load and below), the rotor reaches the pre-synchronization stage quickly—under no-load conditions, 150 ms corresponds to ~660 r/min (pre-synchronization stage) and 220 ms to ~736 r/min (post-synchronization

stage). Switching at 150 ms minimizes both the current surge (31.8 A) and torque ripple while maintaining an acceptable startup settling time (166 ms), achieving the most favorable balance between transient suppression and dynamic response. For intermediate loads (around half-load), a genuine engineering trade-off exists: the rotor reaches ~764 r/min by 300 ms, enabling pre-synchronization switching with a low surge (21.4 A) but a prolonged startup settling time (281 ms); conversely, earliest switching at 30 ms maximizes startup rapidity (startup settling time 235 ms) with an acceptable surge (48.8 A) still below the saturation plateau. For heavy loads (rated-load and above), the pre-synchronization window is not reached until approximately 420 ms, far beyond the practical switching range; because all candidate instants (30–300 ms) occur at low rotor speed (18–280 r/min) where the switching surge remains saturated at ~49–51.5 A, delaying the switch brings no current benefit yet monotonically increases the startup settling time (from 340 ms at 30 ms to instability beyond 500 ms at 300 ms). Rated-load operation should therefore adopt the earliest current-safe switching instant (approximately 30 ms).

The maximum switching surge across all twelve simulated operating points remains below the normal-startup peak current of the proposed machine and the conventional squirrel-cage induction machine, as characterized in Figures 9 and 20. The measured harmonic-starting peak (43.8 A) and normal-starting peak (56.5 A) further corroborate this benchmark, exhibiting less than 5% deviation from the finite-element predictions. Consequently, the allowable current limit for switching-strategy design is set at the normal-startup peak (~57 A) as a design benchmark. The prototype exhibits a measured normal-startup peak of 56.5 A (Figure 20) and a no-load switching peak of approximately 57 A at 30 ms (Table 7). These values are observed peaks during successful startup and switching events, not proven thermal or electrodynamic withstand limits. The maximum switching surge across all twelve simulated operating points (51.54 A) is numerically below this benchmark. This benchmark is adopted as a pragmatic design ceiling, on the basis that the machine has been observed to complete transients at comparable current levels. A formal thermal and electrodynamic withstand limit would require dedicated endurance testing beyond the scope of this study.

The practical implementation comprises two independent rules for distinct load regimes. Rule 1 (speed-threshold switching) applies to light and intermediate loads: switch immediately once the rotor reaches the pre-synchronization stage (approximately 660 r/min corresponding to 150 ms under no-load conditions, and approximately 764 r/min corresponding to 300 ms under half-load conditions). Rule 2 (earliest-current-safe switching) applies to heavy loads: switch immediately after the initial inrush subsides (approximately 30 ms), because delaying the switch brings no current benefit yet monotonically increases the startup settling time. The 150 ms value is the no-load-specific speed-threshold crossing instant, not a universal timeout applicable to all load conditions; the appropriate rule is selected automatically based on the estimated load condition.

The prototype experimental measurements further corroborate the simulation findings. The measured harmonic-starting peak current of 43.8 A and normal-starting peak current of 56.5 A exhibit less than 5% deviation from the finite-element predictions, validating the accuracy of the simulation model. All quantitative conclusions regarding half-load and rated-load switching—including the surge values in Table 5 and the three-zone strategy—are derived from this validated finite-element model. The no-load dynamic switching tests confirm that pre-synchronization switching effectively suppresses transient current inrush, consistent with the simulated trend. The minor deviations between simulation and experimental results—including the mechanical delay of the relay contact (2–3 ms) and amplitude discrepancies for late-switching cases—are caused by manufacturing tolerance, assembly error, and parasitic circuit parameters, which are consistent

with practical engineering characteristics and do not affect the validity of the proposed dual-state operation mechanism.

In terms of broader application prospects, the proposed dual-state operation and adaptive switching optimization framework can be generalized to various intermittent heavy-load drive systems, including mining transportation motors, new energy vehicle auxiliary traction motors, and standby startup electromechanical equipment. Future research directions will focus on the following aspects: first, establishing a precise dynamic mathematical model considering saturation, voltage drop, and switching transient harmonic torque mutation to further improve the prediction accuracy of the low-speed torque behavior under heavy load; second, developing closed-loop speed-triggered intelligent switching control strategies to replace the open-loop time-delay implementation and further improve operational adaptability under variable random loads; third, optimizing the rotor segmentation structure to weaken late-stage harmonic braking torque and expand the efficient operating range of the harmonic starting state.

7. Conclusions

This paper systematically investigates the electromagnetic mechanism, transient performance, and load-adaptive dynamic switching strategy of a novel single-end segmented squirrel-cage induction machine with dual-state operating characteristics. The main conclusions and core innovations are summarized as follows:

First, a dual-mode electromagnetic operating mechanism is revealed based on slot vector theory and the co-rotational auto-resistance principle. The single-main-winding excitation mode generates superimposed multi-order co-rotating harmonic fields to enhance starting torque, while the dual-winding parallel mode realizes complete harmonic offset and pure fundamental-field steady-state operation. The segmented rotor structure actively increases the equivalent rotor resistance under harmonic excitation, fundamentally solving the inherent contradiction between high starting torque and excessive inrush current of conventional induction machines.

Second, the torque–slip characteristics and equivalent circuit models under dual operating states are established. Theoretical analysis and simulation results verify that the proposed machine achieves a 20% higher starting torque multiple (Only the simulation results prove) and nearly 30% lower startup current than conventional squirrel-cage induction machines, effectively improving heavy-load startup capability and transient power supply adaptability.

Third, A load-adaptive recommended switching criterion—pre-synchronization speed window for light loads and current-constraint-bounded early switching for heavy loads—is established based on a unified surge-speed law validated across no-, half-, and rated-load conditions.

Finally, experimental validation demonstrates that the proposed machine maintains excellent steady-state electromagnetic performance consistent with conventional machines while possessing superior transient startup performance and flexible dynamic switching capability. This work provides a complete theoretical basis and engineering reference for the practical application and dynamic recommended control of novel segmented rotor dual-state induction machines in special intermittent heavy-load drive scenarios.

Author Contributions: Conceptualization, M.C. and C.K.; methodology, C.K.; software, M.C.; validation, M.C., C.K. and H.H.; formal analysis, M.C.; investigation, M.C. and D.Y.; resources, X.G.; data curation, H.H.; writing—original draft preparation, M.C.; writing—review and editing, C.K.; visualization, M.C., C.K., H.H., X.G. and D.Y.; supervision, X.G.; project administration, C.K. and X.G.; funding acquisition, C.K. and X.G. All authors have read and agreed to the published version of the manuscript.

Funding: This research was funded by the National Major Science and Technology Project, grant number 2026ZD0810800, and the Open Fund Project of National Key Laboratory of High-Speed Maglev Transportation Technology, grant number SKLM-SFCF-2025-001.

Data Availability Statement: The original contributions presented in this study are included in the article. Further inquiries can be directed to the corresponding author.

Conflicts of Interest: Xinmai Gao was employed by the CRRC Qingdao Sifang Co., Ltd. The remaining authors declare that the research was conducted in the absence of any commercial or financial relationships that could be construed as a potential conflict of interest.

References

1. Habyarimana, M.; Dorrell, D.G.; Musumpuka, R. Reduction of Starting Current in Large Induction Motors. *Energies* **2022**, *15*, 3848. [CrossRef]
2. Shin, Y.; Cho, S.; Lee, J. A Control Strategy for Enhancing Transient-State Stability of Interior Permanent Magnet Synchronous Motors for xEV Applications. *Energies* **2025**, *18*, 4445. [CrossRef]
3. Akbaba, M. A Novel Simple Method for Elimination of DOL Starting Transient Torque Pulsations of Three-Phase Induction Motors. *Eng. Sci. Technol. Int. J.* **2021**, *24*, 728–737. [CrossRef]
4. Chen, J.; Li, J.; Qu, R.; He, K.; Tao, L. A Restart Strategy of a Rotating Induction Machine for Inrush Current Elimination. *IEEE Trans. Ind. Appl.* **2020**, *56*, 4786–4795. [CrossRef]
5. Karakatsanis, T.S. Optimization and Performance Evaluation of PM Motor and Induction Motor for Marine Propulsion Systems. *Appl. Syst. Innov.* **2025**, *8*, 58. [CrossRef]
6. Park, J.-H.; Hong, D.-K. Design and Comprehensive Analysis of Magnetic-geared Permanent Magnet Synchronous Motor for Single-propeller Underwater Propulsion. *IEEE Access* **2025**, *13*, 73486–73497. [CrossRef]
7. Bahrami-Fard, M.; Korrani, M.G.; Rastegar, M.; Fahimi, B. Advanced Startup and Smooth Transition to Sensorless Field Oriented Control for CSI-fed PMSM Drives in Submersible Pumps. *IEEE Trans. Power Electron.* **2025**, *40*, 12402–12415. [CrossRef]
8. Tian, M.; Wang, X.; Yang, Y.; Chen, T.; Yu, H. Research on Starting Performance of Line-start Permanent Magnet Synchronous Motor Based on Pole Changing Winding. *Proc. CSEE* **2017**, *37*, 3287–3297. [CrossRef]
9. Aliabad, A.D.; Mirsalim, M. Analytic Modelling and Dynamic Analysis of Pole-changing Line-start Permanent Magnet Motors. *IET Electr. Power Appl.* **2015**, *9*, 367–376. [CrossRef]
10. Ugale, R.T.; Chaudhari, B.N. Performance Enhancement of Line Start Permanent Magnet Synchronous Motor with A Special Consequent Pole Rotor. *IEEE Trans. Energy Convers.* **2021**, *36*, 1972–1982. [CrossRef]
11. Chen, H.; Gao, C.; Si, J.; Nie, Y.; Hu, Y. A Novel Method for Diagnosing Demagnetization Fault in PMSM Using Toroidal-yoke-type Search Coil. *IEEE Trans. Instrum. Meas.* **2022**, *71*, 1–12. [CrossRef]
12. Xing, Z.; Wang, X.; Yang, Y. A Subdivision Analytical Model for Accurate Prediction, Rapid Positioning and Degree Evaluation of Irreversible Demagnetization of Permanent Magnets in Surface-mounted Permanent Magnet Motors. *IEEE Trans. Energy Convers.* **2026**. [CrossRef]
13. Shabanikia, N.; Nia, A.A.; Tabesh, A.; Khajehoddin, S.A. Weighted Dynamic Aggregation Modeling of Induction Machine-Based Wind Farms. *IEEE Trans. Sustain. Energy* **2021**, *12*, 1604–1614. [CrossRef]
14. Xu, W.; Jian, G.; Weiye, L.; Guobin, L.; Shihu, S.; Yunfeng, H. Advanced Methodologies on Design and Control for Linear Induction Machine and Drive Adopted to Urban Transportation. *CES Trans. Electr. Mach. Syst.* **2022**, *6*, 216–222. [CrossRef]
15. Kan, C.; Zheng, J.; Wang, X.; Wang, Q. Design and Starting Performance Study of A Soft-start Brushless Doubly Fed Machine. *IEEE Trans. Energy Convers.* **2022**, *37*, 97–108. [CrossRef]
16. Kan, C.; Jiang, T.; Jin, K.; Fang, Y.; Zhang, H. Soft-starting Brushless Doubly Fed Machine Winding Design and Magnetic Field Analysis. *IEEE Trans. Ind. Appl.* **2023**, *59*, 1492–1499. [CrossRef]
17. Khaledian, P.; Johnson, B.K.; Hemati, S. Harmonic Mitigation and A Practical Study of Torque Harmonics in Induction Motor Startup. In Proceedings of the 2018 IEEE Power & Energy Society General Meeting (PESGM), Portland, OR, USA, 5–9 August 2018; pp. 1–5. [CrossRef]
18. Kan, C.; Bao, X.; Jin, K.; Li, X.; Wang, Q. Analysis of Magnetomotive Force and Performance During Starting Process of Wound-rotor Brushless Doubly-fed Machine With Combined Multi-harmonic Fields. *Trans. China Electrotech. Soc.* **2020**, *35*, 481–493. [CrossRef]
19. Mallampalli, S.; Zhu, Z.Q.; Mipo, J.C.; Personnaz, S. Six-Phase Pole-Changing Winding Induction Machines With Improved Performance. *IEEE Trans. Energy Convers.* **2021**, *36*, 534–546. [CrossRef]
20. Strous, T.D.; Polinder, H.; Ferreira, J.A. Brushless Doubly-Fed Induction Machines for Wind Turbines: Developments and Research Challenges. *IET Electr. Power Appl.* **2017**, *11*, 991–1000. [CrossRef]

21. Sadeghian, O.; Tohidi, S.; Mohammadi-Ivatloo, B.; Mohammadi, F. A Comprehensive Review on Brushless Doubly-Fed Reluctance Machine. *Sustainability* **2021**, *13*, 842. [CrossRef]
22. Wang, H.; Zhang, F.; Guan, T.; Yu, S. Equivalent Circuit and Characteristic Simulation of a Brushless Electrically Excited Synchronous Wind Power Generator. *Front. Mech. Eng.* **2017**, *12*, 420–426. [CrossRef]
23. Wang, H.; Yu, S.; Jin, S.; Zhang, F. Electromagnetic and Mechanical Design of Module Dual Stator Brushless Doubly-Fed Generator for Offshore Wind Turbine. *IET Renew. Power Gen.* **2021**, *15*, 631–640. [CrossRef]
24. Shi, L.; Jin, S. Direct Power Control and Space Vector Modulation-Based Direct Power Control for Brushless Doubly-Fed Reluctance Generator. *IEEJ Trans. Electr. Electron. Eng.* **2023**, *18*, 1371–1378. [CrossRef]
25. Boldea, I. Electric Generators and Motors: An Overview. *CES Trans. Electr. Mach. Syst.* **2017**, *1*, 25–32. [CrossRef]
26. Ferreira, F.J.T.E.; Baoming, G.; de Almeida, A.T. Reliability and Operation of High-Efficiency Induction Motors. In Proceedings of the IEEE/IAS 51st Industrial & Commercial Power Systems Technical Conference, Calgary, AB, Canada, 5–8 May 2015; pp. 1–8. [CrossRef]
27. Rüncos, F.; Stringari, E.; Gaudeaux, C. Benefits and Drawbacks of Low Inrush Large Induction Squirrel Cage Electric Motors. In Proceedings of the 2018 IEEE Petroleum and Chemical Industry Technical Conference (PCIC), Cincinnati, OH, USA, 24–26 September 2018; pp. 1–8. [CrossRef]
28. Rajkumar, S.; Arunkumar, N.; Sedhuraman, K.; Raghavan, J.V. Finite Element Analysis by High Torque to Weight Ratio for Cage Type Induction Motor Cost Estimation. In Proceedings of the 2024 International Conference on System, Computation, Automation and Networking (ICSCAN), Puducherry, India, 27–28 December 2024; pp. 1–5. [CrossRef]
29. Gundogdu, T.; Suli, S. Role of End-Ring Configuration in Shaping IE4 Induction Motor Performance. *CES Trans. Electr. Mach. Syst.* **2024**, *8*, 245–254. [CrossRef]
30. Cai, M.; Kan, C.; Huang, H.; Yu, Y. Co-rotational/auto-resistance Enhanced Single-end Segmented Rotor Induction Motor for Torpedo-like Propulsion: High Starting Performance. *IEEE Access* **2026**, *14*, 36811–36824. [CrossRef]

Disclaimer/Publisher's Note: The statements, opinions and data contained in all publications are solely those of the individual author(s) and contributor(s) and not of MDPI and/or the editor(s). MDPI and/or the editor(s) disclaim responsibility for any injury to people or property resulting from any ideas, methods, instructions or products referred to in the content.